Available online at www.sciencedirect.com

ScienceDirect

Geochimica et Cosmochimica Acta 169 (2015) 217–235

Geochimica et Cosmochimica Acta

www.elsevier.com/locate/gca

Vivianite is a major sink for phosphorus in methanogenic coastal surface sediments

Matthias Egger [a,*], Tom Jilbert [a,1], Thilo Behrends [a], Camille Rivard [b], Caroline P. Slomp [a]

[a] Department of Earth Sciences – Geochemistry, Faculty of Geosciences, Utrecht University, Princetonplein 9, 3584 CC Utrecht, The Netherlands
[b] European Synchrotron Radiation Facility (ESRF), BP 220, F-38043 Grenoble Cedex, France

Received 25 May 2015; accepted in revised form 8 September 2015; available online 25 September 2015

Abstract

Studies of authigenic phosphorus (P) minerals in marine sediments typically focus on authigenic carbonate fluorapatite, which is considered to be the major sink for P in marine sediments and can easily be semi-quantitatively extracted with the SEDEX sequential extraction method. The role of other potentially important authigenic P phases, such as the reduced iron (Fe) phosphate mineral vivianite ($Fe(II)_3(PO_4)*8H_2O$) has so far largely been ignored in marine systems. This is, in part, likely due to the fact that the SEDEX method does not distinguish between vivianite and P associated with Fe-oxides. Here, we show that vivianite can be quantified in marine sediments by combining the SEDEX method with microscopic and spectroscopic techniques such as micro X-ray fluorescence (μXRF) elemental mapping of resin-embedded sediments, as well as scanning electron microscope–energy dispersive spectroscopy (SEM–EDS) and powder X-ray diffraction (XRD). We further demonstrate that resin embedding of vertically intact sediment sub-cores enables the use of synchrotron-based microanalysis (X-ray absorption near-edge structure (XANES) spectroscopy) to differentiate between different P burial phases in aquatic sediments. Our results reveal that vivianite represents a major burial sink for P below a shallow sulfate/methane transition zone in Bothnian Sea sediments, accounting for 40–50% of total P burial. We further show that anaerobic oxidation of methane (AOM) drives a sink-switching from Fe-oxide bound P to vivianite by driving the release of both phosphate (AOM with sulfate and Fe-oxides) and ferrous Fe (AOM with Fe-oxides) to the pore water allowing supersaturation with respect to vivianite to be reached. The vivianite in the sediment contains significant amounts of manganese (~4–8 wt.%), similar to vivianite obtained from freshwater sediments. Our results indicate that methane dynamics play a key role in providing conditions that allow for vivianite authigenesis in coastal surface sediments. We suggest that vivianite may act as an important burial sink for P in brackish coastal environments worldwide.

1. INTRODUCTION

Phosphorus (P) is an important nutrient controlling primary production in aquatic systems. Throughout the last century, human activities such as the use of agricultural fertilizer, deforestation, increased cultivation, as well as urban and industrial waste disposal have enhanced the input of P into coastal environments (Ruttenberg, 2003). This has led to increased algal blooms in coastal waters, an increased oxygen demand upon the sinking of the organic matter to the seafloor and the expansion of coastal dead zones worldwide (Diaz and Rosenberg, 2008). Burial of potentially bioavailable (i.e. reactive) P in sediments plays a key role

* Corresponding author. Tel.: +31 30 253 3264.
E-mail address: m.j.egger@uu.nl (M. Egger).
[1] Now at: Department of Environmental Sciences, University of Helsinki, Viikinkaari 2a, 00014 Helsinki, Finland.

http://dx.doi.org/10.1016/j.gca.2015.09.012
0016-7037/

in regulating water column P availability, and changes in reactive P burial thus may impact the recovery of coastal waters from eutrophication (Carstensen et al., 2014).

The retention of P in marine sediments is strongly dependent on the chemical form in which P is buried. Degradation of organic matter and reduction of iron (Fe)-(oxyhydr)oxides (henceforth termed Fe-oxides) during early diagenesis typically result in the release of phosphate (HPO_4^{2-}) to the pore water from organic P and Fe-oxide bound P. The dissolved HPO_4^{2-} can then precipitate as authigenic P-bearing phases that may include calcium (Ca)–phosphates such as carbonate fluorapatite (Ca–P) (Ruttenberg and Berner, 1993; Slomp et al., 1996a; Filippelli, 1997), manganese (Mn)–Ca–carbonates (Suess, 1979; Mort et al., 2010; Jilbert and Slomp, 2013) and Fe (II)–phosphates such as vivianite ($Fe_3(II)(PO_4)_2*8H_2O$; Martens et al. (1978), Burns (1997), März et al. (2008)). At the global scale, authigenic Ca–P is assumed to account for ~50% of all P burial in marine sediments, while Fe-bound P (Fe–P) and organic P are assumed to account for ~25% each (Ruttenberg, 2003). At present, the relative contribution of Fe-oxides and vivianite-type Fe(II)–P minerals to the burial of Fe–P is unknown. This is largely due to methodological constraints, as the sequential extraction procedure SEDEX for the determination of P phases in sediments does not allow separation of these Fe–P phases (Ruttenberg, 1992).

Vivianite authigenesis most likely occurs in sediments where sulfate (SO_4^{2-}) concentrations and the input of Fe-oxides are such that not all Fe-oxides are converted to Fe-sulfides and a portion of the Fe-oxides may supply ferrous Fe (Fe^{2+}) for vivianite formation after sulfide has been completely consumed (Ruttenberg, 2003). Lacustrine sediments, naturally rich in Fe-oxides and with low concentrations of SO_4^{2-}, hence provide ideal conditions for the formation of vivianite (Nriagu and Dell, 1974; Fagel et al., 2005; Sapota et al., 2006; Rothe et al., 2014; O'Connell et al., 2015). In marine sediments, the presence of vivianite as an early diagenetic authigenic P phase is generally assumed to be restricted to systems with high sedimentation rates and a relatively high abundance of Fe-oxides (Ruttenberg, 2003). The presence of a sulfate/methane transition zone (SMTZ) may also be particularly conducive to vivianite formation, because pore water Fe^{2+} can accumulate in the absence of sulfide below the SMTZ. Combined with a buildup of pore water HPO_4^{2-} resulting from organic matter remineralization and reductive dissolution of Fe-oxides within the SMTZ, supersaturation with respect to vivianite may be reached (März et al., 2008; Slomp et al., 2013; Hsu et al., 2014).

Marine environments where vivianite formation has been inferred include coastal sediments (Martens et al., 1978; Slomp et al., 2013; Jilbert and Slomp, 2013), deep-sea fan sediments (Burns, 1997; Ruttenberg and Goni, 1997; März et al., 2008) and Fe-rich cold-seep sediments (Hsu et al., 2014). In coastal sediments, vivianite formation has been suggested based on pore water profiles of HPO_4^{2-} and Fe^{2+} and corresponding saturation state calculations (Slomp et al., 2013), or on co-enrichments of Fe and P in sediments (Jilbert and Slomp, 2013). However, direct mineralogical or chemical identification of vivianite in these environments is still lacking. Given the importance of continental margins for marine P burial (Ruttenberg and Berner, 1993; Ruttenberg, 2003), knowledge about the role of vivianite in these sedimentary environments is essential for a better understanding of the global marine P cycle.

In this study, we demonstrate the presence of vivianite in coastal sediments of the Baltic Sea by combining the SEDEX method with a range of microscopic and spectroscopic techniques. Using micro X-ray fluorescence (μXRF) elemental mapping and synchrotron-based X-ray absorption spectroscopy (XAS) of resin-embedded sediment samples, we were able to identify the spatial distribution and size spectrum of different P-bearing phases within the sediment matrix. Specific authigenic P minerals were then isolated through sieving of wet sediment samples and subsequently analyzed by scanning electron microscope–energy dispersive spectroscopy (SEM–EDS) and powder X-ray diffraction (XRD) for conclusive characterization of the mineralogy. We demonstrate that authigenic vivianite constitutes a major P sink at the studied location, which may be typical for many brackish coastal systems worldwide, and should in principle also operate in comparable depositional settings with normal marine salinities. Our results further emphasize that methane (CH_4) plays a key role in facilitating vivianite formation by driving a sink-switching from Fe-oxide bound P to vivianite, as previously hypothesized, but never proven, for a number of fully marine environments (Schulz et al., 1994; Burns, 1997; März et al., 2008).

2. STUDY SITE

The Bothnian Sea is a classic example of an oligotrophic, brackish coastal environment with an average bottom water salinity of 5–6 (Slomp et al., 2013). Organic matter is mainly derived from riverine input and, to a lesser extent, from exchange with the adjacent eutrophic Baltic Proper (Algesten et al., 2006). A major proportion of the organic matter arriving at the sediment surface is therefore relatively refractory (Stockenberg and Johnstone, 1997; Algesten et al., 2006; Leipe et al., 2010). Anthropogenic eutrophication, however, resulted in an increased contribution of autochthonous organic matter over past decades (Fleming-Lehtinen et al., 2008; Fleming-Lehtinen and Laamanen, 2012).

The study site US5B (62°35.17′/19°58.13′) is located in the deepest part of the Bothnian Sea at 214 m depth (Fig. 1) and is characterized by fine-grained sediments and sediment accumulation rates of about 1.3 cm yr^{-1} over the last decade (determined using a Constant Rate of Supply model for ^{210}Pb, see Supplementary Fig. S1). Core sampling was conducted during two research cruises with R/V Aranda in August 2012 and August 2013. Most of the presented data are from sediment cores sampled in 2012 (including pore water and sediment profiles, Fe and P speciation, as well as μXRF elemental mapping and synchrotron XAS analysis on epoxy-embedded sub-cores). Additional sediment from 2013 recovered at the same coring location was taken for analysis of sieved samples by

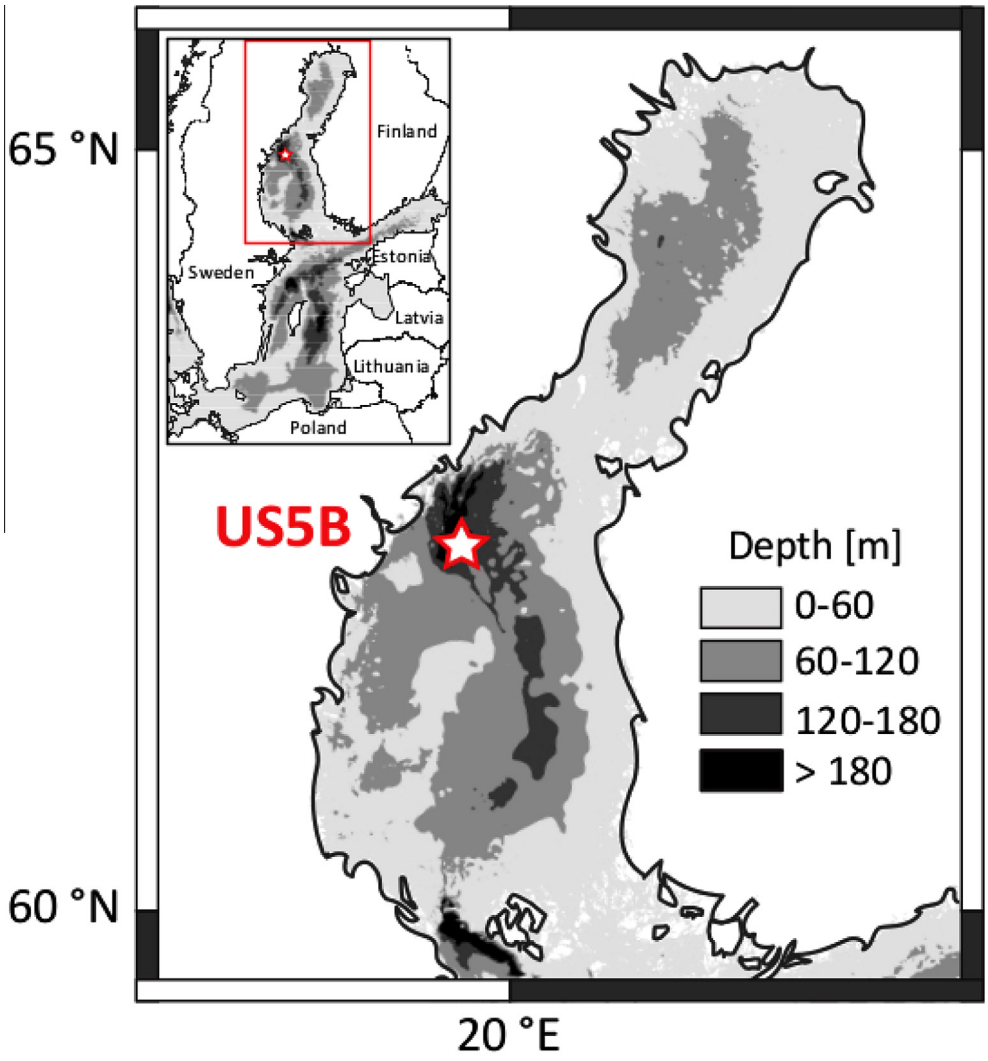

Fig. 1. Location map of the study area. Site US5B (62°35.17′N, 19°58.13′E) is located in the deepest part of the Bothnian Sea at 214 m.

SEM–EDS and powder XRD (see Supplementary Figs. S2 and S3 for pore water and solid-phase data from 2013).

3. ANALYTICAL METHODS

3.1. Bottom water and pore water analysis

3.1.1. Core sampling

Bottom water oxygen, salinity and temperature were measured on board with a CTD (conductivity, temperature and depth) system and an integrated oxygen probe. Sediment cores (50–60 cm of sediment and at least 10 cm of overlying water) were recovered using a GEMAX corer (core diameter 10 cm). One core was immediately inserted into a nitrogen (N_2)-purged glove bag through an airtight hole in the base. A bottom water sample was collected using a 20 mL plastic syringe and the remaining bottom water was removed. The core was then sliced anoxically at 1 cm resolution for the first 0–10 cm and 2 cm resolution for the rest of the core (10–52 cm). For each slice a sub-sample was placed in a pre-weighed glass vial for solid-phase analysis and stored under N_2 in airtight jars at −20 °C. A second sub-sample was transferred to a 50 mL centrifuge tube and centrifuged at 3500 rpm for 20 min. Both the supernatant water from each centrifuged sample and the bottom water sample were filtered through 0.45 μm pore size disposable filters via 20 mL plastic syringes in a glove bag under N_2 and collected in 15 mL centrifuge tubes. The sediment remaining after centrifugation was stored frozen as an additional sediment volume for solid-phase analysis. Filtered pore water samples, including the bottom water sample, were sub-sampled under N_2 for analysis of dissolved HPO_4^{2-}, ammonium (NH_4^+), Fe, Mn, SO_4^{2-} and sulfide ($\sum H_2S = H_2S + HS^-$).

3.1.2. Pore water subsampling

A sub-sample of 0.5 mL was immediately transferred into a glass vial (4 mL) containing 2 mL of 2% zinc (Zn)-acetate solution to precipitate ZnS, which was stored at 4 °C. Sulfide concentrations were then determined spectrophotometrically by complexion of the ZnS precipitate in an acidified solution of phenylenediamine and ferric

chloride (Cline, 1969). The detection limit was <1 μmol/L and the sulfide standard was validated by titration with thiosulfate. Samples for NH_4^+ were stored frozen at −20 °C until colorimetrical determination on a nutrient autoanalyzer (Bran and Luebbe). Sub-samples for total dissolved P, Fe and Mn, of which the latter are assumed to represent Fe^{2+} and Mn^{2+}, were acidified with 10 μL 35% suprapur HCl per mL of sub-sample and stored at 4 °C until analysis by ICP-OES (Perkin Elmer Optima 3000 Inductively Coupled Plasma–Optimal Emission Spectroscopy). Note however, that the dissolved (<0.45 μm) Fe pool likely consists of a mixture of truly dissolved (ionic), organically complexed, colloidal and nanoparticulate Fe (Raiswell and Canfield, 2012). Pore water SO_4^{2-} was analyzed with ion chromatography (IC) (detection limit of <75 μmol/L) and compared well with total sulfur (S) measured by ICP–OES. The alkalinity was determined by titrating 1 mL of untreated sub-sample with 0.01 M HCl. Samples for dissolved inorganic carbon (DIC) analysis were collected in 5 mL headspace vials and poisoned with 10 μL of saturated $HgCl_2$ (only for 2013). DIC analysis was performed using an AS-C3 analyzer (Apollo SciTech), which consists of an acidification and purging unit in combination with a LICOR-7000 CO_2/H_2O Gas Analyzer. Quality assurance involved regular analysis of Certified Reference Materials obtained from the Scripps Institution of Oceanography (Dickson et al., 2003).

3.1.3. Methane sampling

Samples for CH_4 analysis were taken from a core with pre-drilled holes directly upon core retrieval. Precisely 10 mL wet sediment was extracted from each hole and immediately transferred into a 65 mL glass bottle filled with saturated NaCl solution. Each bottle was sealed with a black rubber stopper and a screw cap and was subsequently stored upside-down. A volume of 10 mL N_2 was injected into the bottle and a subsample of the headspace was collected with a gas-tight syringe. Subsequently, CH_4 concentrations were determined after injection into a Thermo Finnigan Trace GC gas chromatograph (Flame Ionization Detector).

3.2. Bulk sediment analysis

Sediment samples were freeze-dried, powdered and ground in an agate mortar inside an argon (Ar)-filled glove box and split into oxic and anoxic fractions. Samples from the oxic fraction were used for total elemental and organic carbon (C_{org}) analyses, whereas anoxic splits were taken for sediment P and Fe speciation to avoid oxidation artefacts (Kraal et al., 2009; Kraal and Slomp, 2014).

3.2.1. Total elemental composition and organic carbon

A split of about 125 mg of freeze-dried sediment was dissolved in 2.5 mL HF (40%) and 2.5 mL of $HClO_4/HNO_3$ mixture, in a closed Teflon bomb at 90 °C over night. The acids were then evaporated at 160 °C (not to complete dryness) and the resulting gel was subsequently dissolved in 1 M HNO_3 at 90 °C during another night. Finally, total elemental concentrations were determined by ICP–OES. The coefficient of variation (CV) of the concentrations, obtained from replicate measurements of standard solutions, was less than 5% for all analyzed elements. The accuracy was evaluated by including internal laboratory reference standards in the analysis and the deviation from the nominal concentrations was less than 5%. A second split of 0.3 g freeze-dried sediment was used to determine the C_{org} content using an elemental analyzer (Fison Instruments model NA 1500 NCS) following carbonate removal from the sediment with 1 M HCl (Van Santvoort et al., 2002) (CV and accuracy <2% based on an atropine/acetanilide standard calibration and checked against internal laboratory standard sediments).

3.2.2. Sediment P fractionation

To determine the solid-phase partitioning of P, aliquots of 0.1 g dried sediment were subjected to the SEDEX sequential extraction procedure after (Ruttenberg, 1992), as modified by (Slomp et al., 1996a), but including the first $MgCl_2$ step. Sediment P was fractionated as follows: (i) exchangeable-P (extracted by 1 M $MgCl_2$, pH 8, 0.5 h), (ii) Fe-oxide bound P (extracted by citrate-bicarbonate-dithionite (CDB), pH 7.5, 8 h, followed by 1 M $MgCl_2$, pH 8, 0.5 h), (iii) authigenic Ca–P (including carbonate fluorapatite, biogenic hydroxyapatite and $CaCO_3$-bound P, extracted by Na-acetate buffer, pH 4, 6 h, followed by 1 M $MgCl_2$, pH 8, 0.5 h), (iv) detrital Ca–P (extracted by 1 M HCl, 24 h) and (v) organic P (after ashing at 550 °C for 2 h, extracted by 1 M HCl, 24 h). Sediments were shielded from oxygen inside an Ar-filled glovebox until step 3 of the SEDEX procedure to eliminate the potential conversion of Ca–P to Fe-bound P due to pyrite oxidation upon oxygen exposure (Kraal et al., 2009; Kraal and Slomp, 2014). Dissolved HPO_4^{2-} in the CDB rinse was analyzed by ICP–OES. For all other rinses, HPO_4^{2-} was determined colorimetrically (Strickland and Parsons, 1972) on a Shimadzu spectrophotometer by the ammonium heptamolybdate – ascorbic acid method (CV and accuracy <2%, based on calibration to standard solutions and checked against internal laboratory standard sediments).

3.2.3. Sediment Fe fractionation

To investigate the solid-phase partitioning of Fe, a second 50 mg aliquot of dried sediment was subjected to a sequential extraction procedure for Fe (Poulton and Canfield, 2005). Sediment Fe was fractionated into (i) carbonate associated Fe ("Fe_{carb}", including siderite and ankerite, extracted by 1 M Na-acetate brought to pH 4.5 with acetic acid, 24 h), (ii) easily reducible (amorphous) oxides ("Fe_{ox1}", including ferrihydrite and lepidocrocite, extracted by 1 M hydroxylamine-HCl, 24 h, and corrected for dissolution of acid volatile sulfur (AVS) (Egger et al., 2015)), (iii) reducible (crystalline) oxides ("Fe_{ox2}", including goethite, hematite and akagenéite, extracted by Na-dithionite buffer, pH 4.8, 2 h) and (iv) Fe in recalcitrant oxides (mostly magnetite, "Fe_{mag}", extracted by 0.2 M ammonium oxalate/0.17 M oxalic acid solution, 2 h). Measured concentrations from duplicate analysis deviated by less than 5%.

A third 0.5 g aliquot of dried sediment was used to sequentially determine the amount of FeS (AVS, using

6 M HCl) and FeS_2 (chromium reducible sulfur, CRS, using acidic chromous chloride solution) via the diffusion-based approach described by Burton et al. (2008) using iodometric titration of the alkaline Zn-acetate trap. Measured concentrations from duplicate sample extractions varied by less than 8% for CRS and less than 10% for AVS. The difference between total Fe measured after digestions with HF–$HClO_4$–HNO_3 and the sum of the six phases described above (i.e. $Fe_{carb} + Fe_{ox1} + Fe_{ox2} + Fe_{mag} + Fe_{FeS2} + Fe_{FeS}$) gives an estimate of the remaining poorly reactive sheet silicate Fe and unreactive silicate Fe ("$Fe_{PRS\ \&\ U}$"). For simplicity, the Fe_{ox1} and Fe_{ox2} fractions were summed and henceforth referred to as total sedimentary Fe-oxides.

3.3. Characterization of Fe–Mn–P aggregates mineralogy

3.3.1. Epoxy embedding and Desktop μXRF mapping

Vertically intact sub-cores from a sediment GEMAX core were embedded with epoxy resin under inert atmosphere for elemental microanalysis (Jilbert et al., 2008; Jilbert and Slomp, 2013). In total, 8 sub-cores with a length of 7 cm each were taken. After curing, epoxy-embedded sub-cores were opened perpendicular to the plane of sedimentation with a rock saw. The freshly exposed internal surface was pre-drilled with a grid of holes for navigation and polished with a 0.3 μm alumina powder. Exposure time to oxygen was kept as short as possible during sample treatment and samples were stored in a glovebox or gas-tight aluminum bags between treatment steps, in order to preserve the redox-sensitive chemical composition (Kraal et al., 2009; Kraal and Slomp, 2014). Elemental maps of the sub-cores were then collected using a Desktop EDAX Orbis μXRF analyzer (Rh tube at 30 kV, 500 μA, no filter, 300 ms dwell time, poly-capillary lens providing a 30 μm spot size) using a 30 μm lateral step.

3.3.2. X-ray absorption spectroscopy (XAS)

Selected Fe-, Mn- and P-rich regions from the Desktop μXRF maps of sediment samples from approximately 0.5 cm, 13 cm, 30 cm and 48 cm depth were further investigated on the ID21 beamline (Salomé et al., 2013) at the European Synchrotron Radiation Facility (ESRF) in Grenoble, France, during beamtime in April 2013 and April 2014. Monochromator energy was calibrated against the maximum intensity of the first derivative of tricalcium phosphate at 2.1523 keV for P, of a Fe foil at 7.11198 keV for Fe and of a Mn foil at 6.53862 keV for Mn. The X-ray beam was focused to 1.05 × 0.45 (horizontal × vertical) μm at the P-edge and to 0.35 × 0.80 μm at the Fe- and Mn-edges with a Kirkpatrick-Baez mirrors system. High-resolution elemental maps (1 μm lateral step size) of the pre-identified P enrichments were collected at 2.3 keV to target specific regions of high P counts with X-ray absorption near-edge structure (XANES). Maps were also collected at 7.5 keV to display Fe, Mn and P correlations. XANES spectra were collected at the Fe, Mn, and P K-edges in fluorescence mode, in order to determine the redox state and mineralogy of the P enrichments. The analyses were conducted under vacuum and at room temperature. For each sample, between 5 and 10 spectra were collected within the corresponding energy range (Fe: 7.00–7.65 keV, Mn: 6.50–6.90 keV, P: 2.13–2.46 keV) and averaged to improve the signal-to-noise ratio, with a step of 0.59 eV, 0.40 eV and 0.39 eV for Fe, Mn and P, respectively and acquisition time of 0.1 s per step. The ATHENA software package (Ravel and Newville, 2005) was used for standard XANES background subtraction and edge step normalization.

Additional Fe-, Mn- and P-rich regions from the Desktop μXRF map from 48 cm depth, as well as sieved sediment fractions from a core taken in 2013 (22 cm and 58 cm depth) were further investigated on the I18 beamline at the Diamond Light Source (DLS) in Oxfordshire, UK, during beamtime in March 2015. These results are presented in the Supplementary Information only.

3.3.3. Scanning electron microscopy (SEM)

The morphology of Fe-, Mn- and P-rich particles and their chemical composition were investigated by SEM–EDS. Wet sediment samples from a core taken in 2013 were sieved through a 38 μm sieve, washed 5 times in a sonic bath (3 min) with oxygen-free UHQ water, and dried under an inert atmosphere at room temperature. Aliquots of sieved and dried samples from different sediment depths (0.25 cm, 2.5 cm, 5.5 cm, 11 cm, 15 cm, 22 cm, 30 cm and 58 cm) were mounted on aluminum sample holders using double-sided carbon tape. Measurements were performed on a JEOL JXA 8600 Superprobe with Noran Voyage automation, 15 kV accelerating voltage, Si/Li detector, and 1 μm beam in backscatter mode imaging (BEI). EDS analysis was carried out using a probe current of 1 nA and an acquisition time of 50 s (live time) and data were collected on the 0–20 keV energy range.

3.3.4. Powder X-ray diffraction (XRD)

A fraction of the sieved (>38 μm) sediment sample from directly below the SMTZ (22 cm depth, core 2013) was ground in an agate mortar inside an Ar purged glovebox. XRD analysis of the sample and reference material was performed using Cobalt (Co) Kα radiation on a Bruker D2 diffractometer over a 5–85° 2θ range with a step size of 0.026° and a measurement time of 0.4 s per step. Some of the spectra were shifted because the sample was not perfectly located in the zero plane. This shift was corrected by using the 1 0 1 quartz diffraction peak to 31.05 2θ Co Kα.

3.3.5. Preparation of reference samples

Vivianite was synthesized under an inert (Ar) atmosphere as described by Rouzies and Millet (1993) and Dijkstra et al. (2014). No other crystalline phases than vivianite were identified by XRD-analysis. 2-line ferrihydrite was prepared after Schwertmann and Cornell (2000) by mixing a solution of $Fe(NO_3)$ (40 g in 500 mL) with 330 mL 1 M KOH and co-precipitated with 0.1 M PO_4 (1.36 g KH_2PO_4 in 100 mL). The Mn phosphate and Mn_2O_3 were purchased from Alfa Aesar and hureaulite ($(Mn^{2+})_5(PO_3OH)_2(PO_4)_2{*}4H_2O$) and bixbyite ($(Mn^{3+}, Fe^{3+})_2O_3$) were identified as major crystalline components by XRD.

4. RESULTS

4.1. Pore water and sediment profiles

Vertical pore water profiles of SO_4^{2-}, CH_4 and sulfide (Fig. 2) reveal a shallow SMTZ around a depth of 4 to 9 cm, where anaerobic oxidation of CH_4 coupled to SO_4^{2-} reduction (SO_4-AOM) results in the depletion of pore water SO_4^{2-} and CH_4 and in the accumulation of dissolved sulfide, as described previously for site US5B (Egger et al., 2015). Note that the SMTZ was located slightly deeper in 2013 (~15–20 cm) when compared to 2012 (~4–9 cm) due to spatial heterogeneity (see Supplementary Fig. S4). Alkalinity is generally elevated with respect to the Redfield C/NH_4^+ ratio of 106:16 likely due to the production of HCO_3^- during SO_4-AOM. Pore water HPO_4^{2-} shows a distinct peak of up to ~300 μmol/L around the SMTZ and decreases to ~150 μmol/L at depth. Dissolved Fe^{2+} reaches a maximum of ~20 μmol/L at 2.5 cm depth and builds up to concentrations greater than 1800 μmol/L in the pore water below the SMTZ. Dissolved Mn^{2+} shows a strong increase from 0 to 1.5 cm depth and levels off at 500 μmol/L around the SMTZ, below which an almost linear increase to about 1 mmol/L at depth is observed. Dissolved NH_4^+ increases with depth to about 3 mmol/L at the bottom of the core.

The SMTZ is further characterized by a distinct enrichment in total sedimentary S of up to 700 μmol/g (Fig. 3). C_{org} decreases from 3.1 wt.% at the sediment surface to about 2.5 wt.% below 7 cm depth. Throughout the whole core, total Fe is high and varies between 1000 and 1400 μmol/g. Total Mn contents decline from ~140 μmol/g close to the sediment surface to ~35 μmol/g at depth.

Total concentrations of P range from ~40 to 90 μmol/g, with the lowest sedimentary P content observed within the SMTZ (Fig. 4a). Total concentrations of P measured after $HF–HClO_4–HNO_3$ digestion show similar values when compared to the amount of P recovered during the SEDEX extraction (difference < 7%). In general, Fe-bound P accounts for up to ~60% of total P and thus represents the most important burial sink for P (Table 1). Around the SMTZ, however, the amount of Fe-bound P is lower with a percentage of around 30%. Authigenic Ca–P concentrations are mostly constant throughout the core and contribute to ~20% of the total burial of P below the SMTZ. Organic P initially declines from about 10 μmol/g at the sediment surface and levels off at ~8 μmol/g below the SMTZ, accounting for about 15% of the reactive sedimentary P. Exchangeable P shows a small peak of 4 μmol/g at 2.5 cm depth. Detrital P generally stays below 5 μmol/g throughout the core, contributing to about 5% of the total P burial below the SMTZ.

The sum of sequentially extracted Fe ("reactive" Fe) generally accounts for about 40% of total Fe, but reaches values of up to ~ 60% around the SMTZ (Table 1). Fe-oxides are the most dominant reactive Fe phase above the SMTZ (~70% of the total reactive Fe at the sediment surface), while Fe-sulfides (~70%) and Fe-carbonates

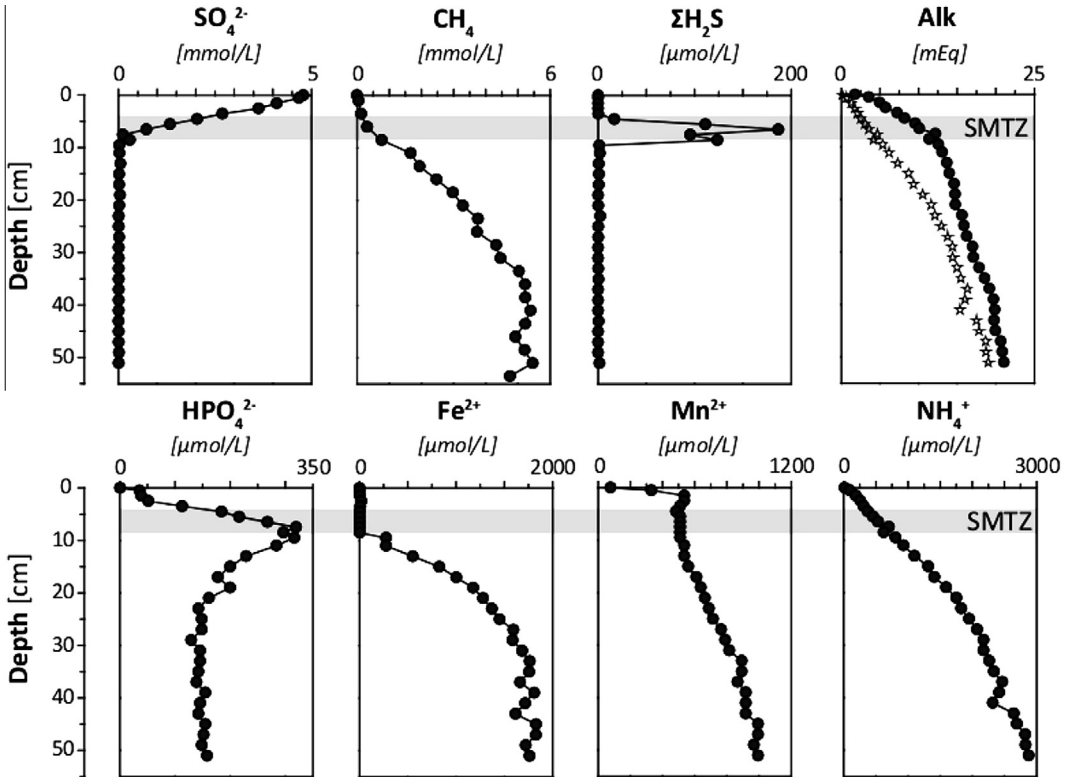

Fig. 2. Pore water profiles of key components for 2012 ($\sum H_2S = H_2S + HS^-$). Grey bar indicates sulfate/methane transition zone (SMTZ). White stars represent estimated alkalinity (Alk) based on the Redfield C/NH_4^+ ratio of 106:16.

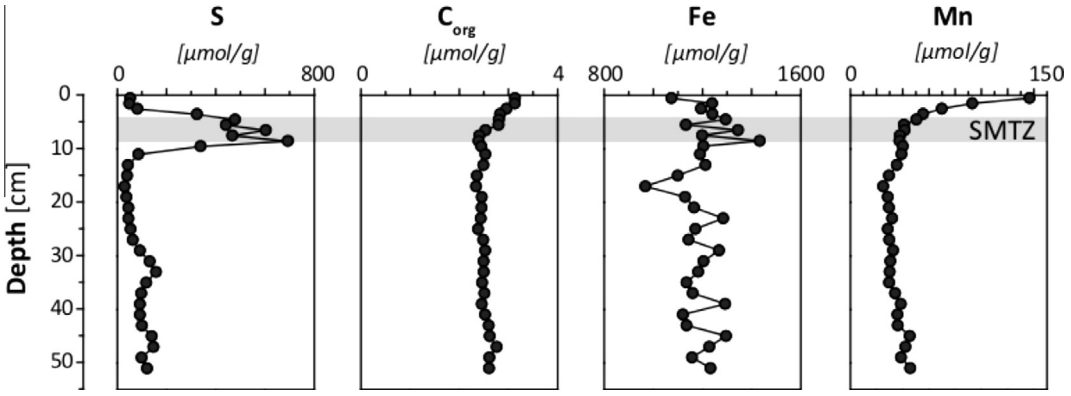

Fig. 3. Solid phase sediment profiles of sulfur (S), organic carbon (C_{org}), Fe and Mn for 2012. Grey bar indicates the position of the SMTZ.

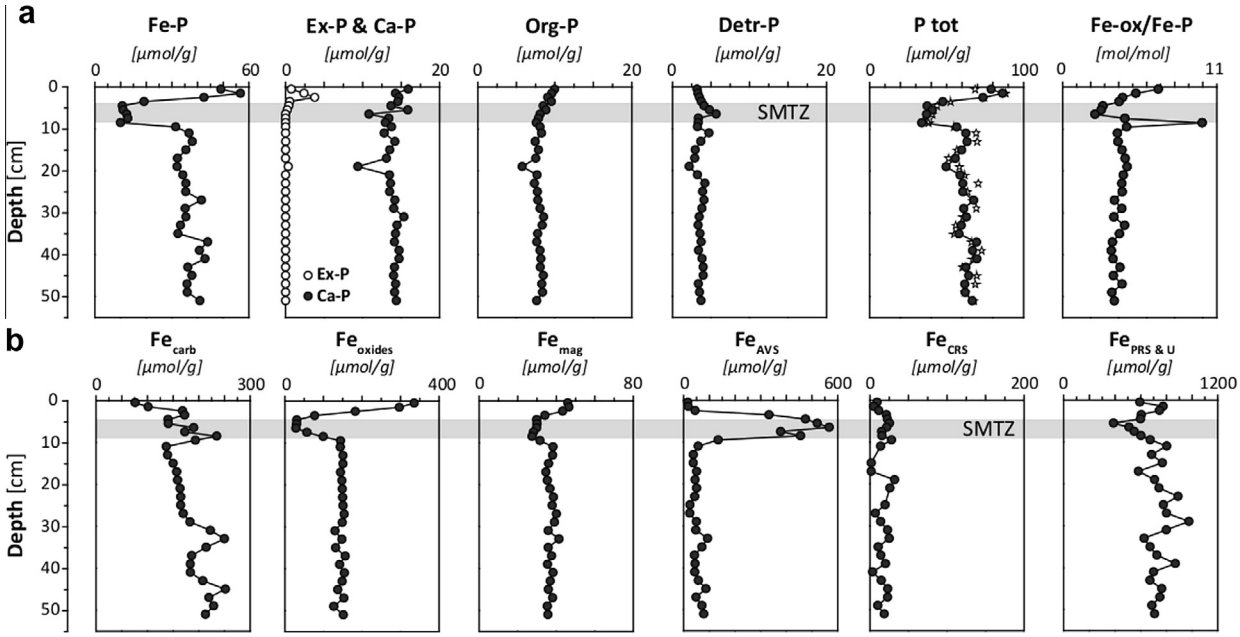

Fig. 4. (a) SEDEX phosphorus speciation results, showing Fe-bound P (Fe–P), exchangeable-P (Ex-P), authigenic P (Ca-P), organic P (Org-P) and detrital P (Detr-P). The white stars represent total P as determined by ICP–OES after total digestion with HF. (b) Fe extraction results including carbonate associated Fe (Fe_{carb}), Fe-oxides (Fe_{oxides}), magnetite Fe (Fe_{mag}), Fe_{AVS} (acid volatile sulfide, typically used as a measure for FeS), Fe_{CRS} (chromium reducible sulfur, assumed to represent FeS_2) and poorly reactive and unreactive silicate Fe ($Fe_{PRS\ \&\ U}$). Fe-ox/Fe–P represents the molar ratio of Fe associated with Fe-oxides to Fe-bound P. Grey bar indicates the position of the SMTZ.

(~20%) account for most of the reactive Fe in the sulfidic zone. Below the SMTZ, Fe-oxides and Fe-carbonates are the predominant reactive Fe phases, each accounting for ~30% to 40% of total reactive Fe. Concentrations of magnetite are lowest at the SMTZ (~30 µmol/g) and generally stay around 40 µmol/g at depth, contributing to ~8% of reactive Fe burial. Fe-sulfides are dominated by AVS (FeS) with only minor contributions from CRS (FeS_2) (Fig. 4b).

4.2. Spatial distribution of P within sediment matrix

The Desktop µXRF maps of Fe, P and Mn on the internal surfaces of epoxy resin-embedded sediment sub-cores reveal distinct changes in elemental distribution with depth (Fig. 5). Close to the sediment/water interface (SWI) (~0.5 cm), P is mostly diffusely distributed with some P enrichments that are visible as single pixels or small clusters of ~4 × 4 pixels at the 30 µm resolution of the Desktop µXRF maps. Some Fe enrichments correspond to enrichments in P or Mn. In general, however, the presence of diffusely distributed Fe oxides and Fe in clay minerals, and the deeper penetration of the X-ray beam for Fe in comparison to lighter elements such as P, generate consistently high counts throughout the Fe map at this depth.

Directly below the SMTZ (~13 cm), large enrichments (>500 µm) in Fe are observed, in correlation with the presence of S (see Supplementary Fig. S5), indicating authigenic Fe-sulfide formation. However, most of the smaller Fe enrichments show no connection with S, but are highly

Table 1
Average P and Fe species contribution for sediments above, within and below the SMTZ. See Fig. 4 for terminology of the different fractions.

[μmol/g]	Ex-P	Fe–P	Ca–P	Org-P	Detrital-P	Total P	
P speciation results							
Above SMTZ (0–3.5 cm)	1.9	41.9	14.9	9.6	3.4	71.6	
Within SMTZ (4.5–8.5 cm)	0.1	11.4	13.3	8.2	4.3	37.3	
Below SMTZ (9.5–51 cm)	0.0	36.5	13.8	7.9	3.6	61.8	
[%]	Ex-P	Fe–P	Ca–P	Org-P	Detrital-P	Total P	
Above SMTZ (0–3.5 cm)	2.6	58.5	20.8	13.4	4.8	100.0	
Within SMTZ (4.5–8.5 cm)	0.4	30.5	35.8	22.0	11.4	100.0	
Below SMTZ (9.5–51 cm)	0.0	59.0	22.4	12.7	5.8	100.0	
[μmol/g]	Fe_{carb}	Fe_{oxides}	Fe_{mag}	Fe_{AVS}	Fe_{CRS}	$Fe_{PRS\&U}$	Total Fe
Fe speciation results							
Above SMTZ (0–3.5 cm)	129.4	222.8	42.4	102.2	11.6	678.4	1186.8
Within SMTZ (4.5–8.5 cm)	175.5	49.2	29.0	478.7	19.9	528.4	1280.8
Below SMTZ (9.5–51 cm)	188.1	145.8	36.9	55.6	23.3	743.4	1193.1
[% total Fe]	Fe_{carb}	Fe_{oxides}	Fe_{mag}	Fe_{AVS}	Fe_{CRS}	$Fe_{PRS\&U}$	Total Fe
Above SMTZ (0–3.5 cm)	10.9	18.8	3.6	8.6	1.0	57.2	100.0
Within SMTZ (4.5–8.5 cm)	13.7	3.8	2.3	37.4	1.6	41.3	100.0
Below SMTZ (9.5–51 cm)	15.8	12.2	3.1	4.7	2.0	62.3	100.0
[% reactive Fe]	Fe_{carb}	Fe_{oxides}	Fe_{mag}	Fe_{AVS}	Fe_{CRS}	Total reactive Fe	
Above SMTZ (0–3.5 cm)	25.4	43.8	8.3	20.1	2.3	100.0	
Within SMTZ (4.5–8.5 cm)	28.3	6.5	3.9	63.6	2.7	100.0	
Below SMTZ (9.5–51 cm)	41.8	32.4	8.2	12.4	5.2	100.0	

correlated with P and Mn (see, for example, points P3, P4 and P6 in Figs. 5 and 6). Compared to the Desktop μXRF maps collected close to the SWI, P and Mn show a less diffuse distribution with many circular 50–100 μm enrichments. Almost all of the brightest pixels in the P map are also bright in the corresponding maps of Fe and Mn, suggesting the presence of Fe–Mn–phosphates. With increasing sediment depth (at ~30 cm and ~48 cm), these Fe–Mn–P enrichments become more abundant, while the Fe–S enrichments decline.

4.3. Mineralogy and chemical composition of P enrichments

Synchrotron-based μXRF maps of selected P-rich regions from the Desktop μXRF maps show 50–100 μm sized P-, Fe- and Mn-rich aggregates in sediments below the SMTZ (Fig. 6). μXANES spectra collected on these aggregates at the P, Fe and Mn K-edge are shown in Fig. 7. In general, the normalized μXANES spectra at any given depth were very similar and showed only minor variations for the different Fe–Mn–P enrichments within an epoxy-embedded sub-core sample (Supplementary Fig. S6). The normalized spectra were thus merged together to represent an average sample spectrum for the P enrichments in the corresponding depth (Fig. 7).

4.3.1. P-XANES

The white lines collected at the P K-edge all peak around 2153.5 eV (Fig. 7a). The white line position and the general shape of the P-XANES spectra correspond to those obtained for P reference materials in which P is associated with Fe, including vivianite and ferrihydrite co-precipitated with phosphate (Fh-PO_4). White line position and shape of the P-XANES spectra were distinctly different to those obtained for reference materials in which P is bound to Ca containing minerals such as apatite or co-precipitated in carbonates (Ingall et al., 2011; Kraal et al., 2015). Despite the general similarity, P-XANES spectra of the Fe–Mn–P enrichment at 0.5 cm depth clearly differ from those for enrichments below the SMTZ. This specifically holds with respect to the amplitude of the white line. The different amplitude of the peak at 2153.5 eV could be attributed to self-absorption. Self-absorption attenuates the emitted fluorescence and the amplitude of features in XAS spectra collected in fluorescence mode. The extent of self-absorption depends on the concentration of the element in the sample and comparison of P-XANES spectra collected in fluorescence and transmission mode confirms (data not shown) that self-absorption is more pronounced when analyzing vivianite than Fh-PO_4. Hence, the different amplitude of the white line peak could indicate that P is more concentrated in the enrichments below the SMTZ than at 0.5 cm depth. However, the P-XANES spectra at 0.5 cm depth do not exhibit a pre-edge feature around 2149 eV, as is observed in the Fh-PO_4 spectrum and which is indicative for the presence of Fe(III) (Ingall et al., 2011) (Fig. 7i). Although the spectra of enrichments below the SMTZ bear great resemblance to the vivianite reference spectrum, the characteristic oscillation around 2161–2166 eV is missing in the spectrum for Fe–Mn–P aggregates from 13 cm and 30 cm depth, but is present in the P-XANES collected from 48 cm depth (Fig. 7ii), however.

P-XANES spectra collected at the DLS from enrichments in 48 cm depth were similar to those collected at the ESRF but showed a more pronounced pre-edge feature around 2149 eV (Supplementary Fig. S7i) and no

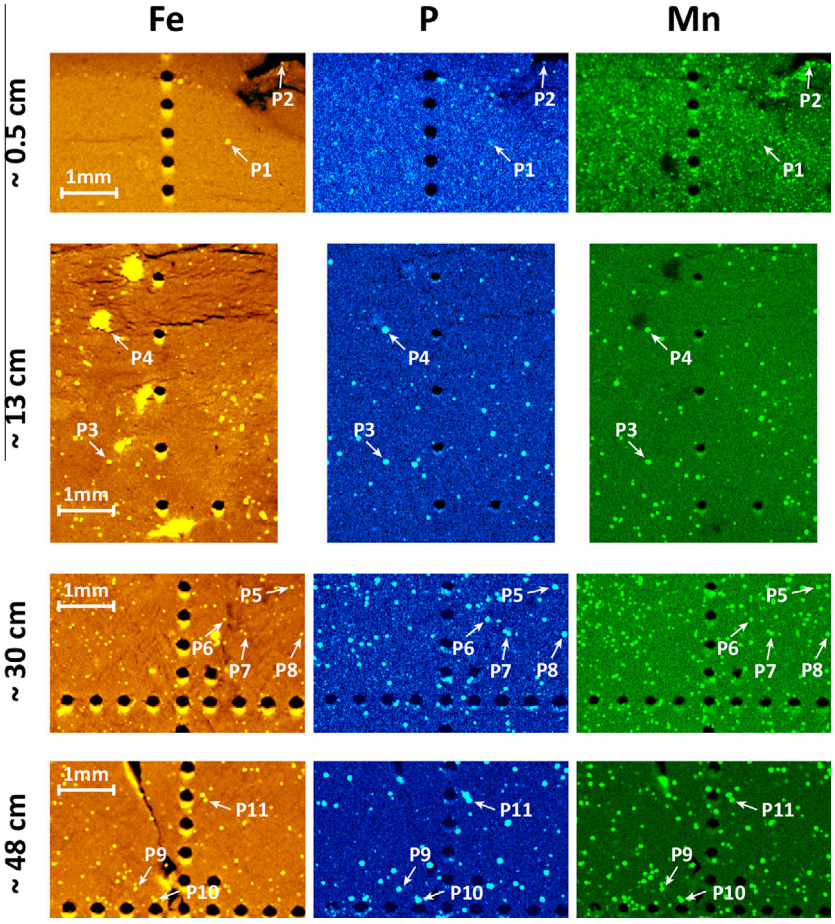

Fig. 5. Desktop μXRF maps (30 μm resolution) of Fe, P and Mn on the internal surface of epoxy-embedded sediment sub-cores. The maps are presented in true vertical orientation. Note that the grid at 13 cm was drilled with 1 mm spacing, while the other samples were pre-drilled with 0.5 mm resolution. Color scaling is based on the count intensity range within the mapped area and adjusted for brightness and contrast to optimize the visualization of features. The arrows indicate examples of coincident enrichments of Fe, P and Mn that were further investigated by synchrotron-based focused-beam μXRF mapping (Fig. 6) and XAS (Fig. 7). (For interpretation of the references to color in this figure legend, the reader is referred to the web version of this article.)

characteristic vivianite oscillation. However, P-XANES obtained for the blue crystals analyzed in the sieved sediment samples do not differ significantly from the P-XANES spectra collected on the resin-blocks at ESRF from 13 cm and 30 cm depth, with the exception of the more pronounced pre-edge feature (Supplementary Fig. S7ii).

4.3.2. Fe-XANES

In general, Fe-XANES spectra of Fe–Mn–P enrichments from above the SMTZ are distinctly different from those collected from below the SMTZ. However, in contrast to the P-XANES spectra, the Fe-XANES spectra from the enrichments do not closely resemble those from vivianite or Fh-PO_4 or any other analyzed reference material. Nevertheless, the difference in the spectra of Fh-PO_4 and vivianite can be used to infer differences in Fe speciation in enrichments above and below the SMTZ. Fe-XANES spectra for Fh-PO_4 and vivianite differ in the location of their corresponding white lines, with peaks observed at 7132 eV for Fh-PO_4 and at 7127 eV for vivianite (Fig. 7b). White lines collected for the Fe–Mn–P enrichments at the ESRF fall between the spectra for Fh-PO_4 and vivianite, i.e. around 7130.5 eV (Fig. 7iv) and suggest the presence of Fe in both oxidation states. The edge position is an indicator for the Fe redox state (Wilke et al., 2001) and points toward a dominant contribution of Fe(II) over Fe(III) (Fig. 7iii) in the spectra of all enrichments, with a larger fraction of Fe(III) in enrichments from 0.5 cm depth. The pre-edge feature can also be used to infer the Fe redox state. Fe-XANES of Fh-PO_4 show a characteristic pre-edge peak around 7114.5 eV, indicating the presence of Fe(III) (Wilke et al., 2001). By contrast, the vivianite spectrum displays a double pre-edge peak with a first peak at 7112 eV, attesting for the presence of Fe(II) and a second, less intensive one at 7114.5 eV. The Fe-XANES spectrum collected from enrichments close to the sediment surface, i.e. from 0.5 cm depth, shows a pre-edge peak at 7114.5 eV, but less pronounced compared to Fh-PO_4. Samples from below the SMTZ depict a double pre-edge feature at 7112 eV and at 7114 eV, confirming that Fe in the samples from below the SMTZ has a larger fraction of Fe(II). Fe K-edge XANES thus appears to be more sensitive to oxidation state than P K-edge

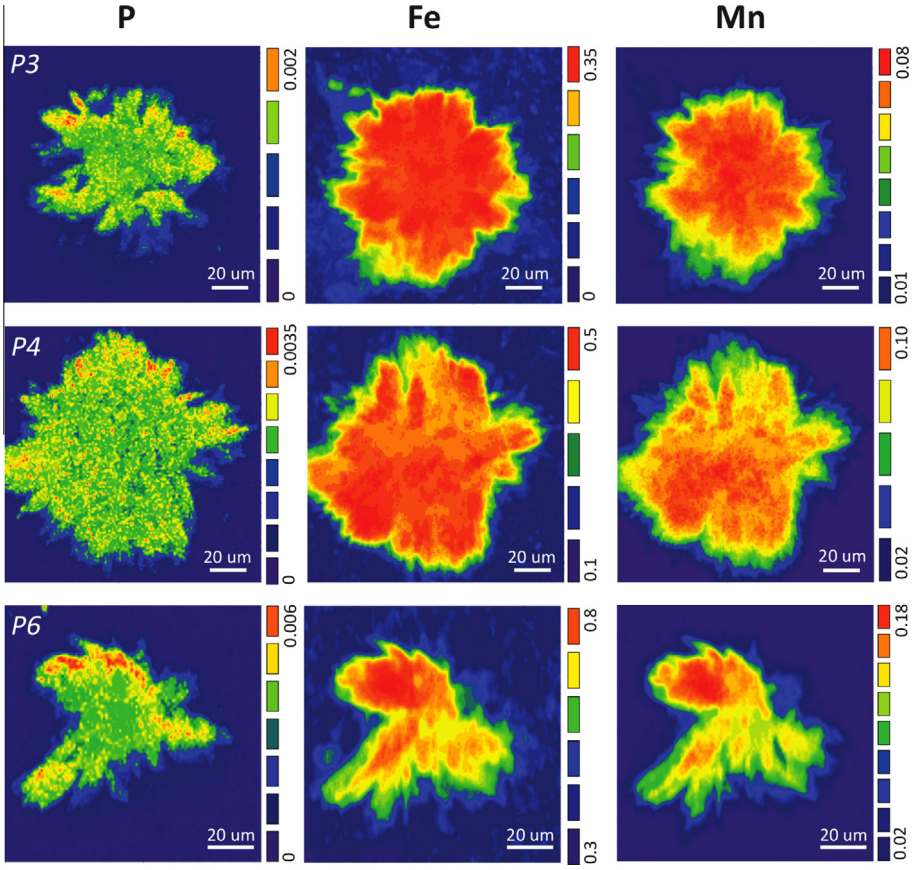

Fig. 6. Synchrotron-based focused-beam μXRF maps of selected pre-identified P enrichments from below the SMTZ (P3, P4 and P6, Fig. 5) mapped at 7.5 keV and 1 μm resolution. Color bars indicate relative count intensities that are linearly scaled to XRF count intensities. (For interpretation of the references to color in this figure legend, the reader is referred to the web version of this article.)

XANES, where no characteristic Fe(III) pre-edge feature is detected for the P enrichment at 0.5 cm depth. Samples analyzed at the DLS have white line and pre-edge peaks similar to Fh-PO_4 and a post-edge shoulder at 7137 eV (Supplementary Fig. S7b).

The impossibility to assign the Fe-XANES spectra of the enrichments to vivianite, Fe–PO_4 or any other analyzed reference phase is most likely a consequence of the presence of Fe in different phases in the analyzed sample volume. The sample volume, which is probed with the focused beam, is larger at the Fe K-edge than at the P K-edge due to the larger penetration depth of the beam at higher energy. A satisfactory fit of the measured Fe-XANES spectra by linear combination of reference spectra is possible but the results are not presented here, as the set of reference materials might not include all the Fe phases in the sample. In particular, various Fe-silicates could contribute significantly to the measured Fe-XANES spectrum.

4.3.3. Mn-XANES

Mn-XANES spectra of enrichments from below the SMTZ show a great similarity to the spectrum of hureaulite, with white line peaks at 6552 eV (Fig. 7c) and differ considerably from spectra of other Mn(II) containing phases such as rhodochrosite ($MnCO_3$) and Mn(II)-sulfides. The Mn-XANES spectrum of the sample close to the sediment surface represents a phase with Mn in a higher oxidation state. This conclusion is based on the comparison of the positions of the edge, the white line and the pre-edge features to those for Mn-oxides. The position of the white line is similar to that of Mn(III) in bixbyite, with a peak around 6559 eV. All samples show a pre-edge peak at 6540 eV, which is shifted toward higher energy for the sample from 0.5 cm depth, confirming that the shallower sample is more oxidized when compared to samples from below the SMTZ (Fig. 7v). Mn-XANES spectra collected at DLS all show a more pronounced pre-edge peak at 6540 eV (Supplementary Fig. S7c).

4.3.4. SEM–EDS

Examination of the sieved sediment with a light microscope revealed that transparent to light blue crystals were present in sediments from below the SMTZ (Fig. 8a), with shapes similar to vivianite crystals found in sediments of Lake Biwa, Japan (Nakano, 1992), while no such crystals were observed in samples from above the SMTZ by light microscopy nor SEM. Scanning electron micrographs of these blue crystals show spherical aggregates (~50–100 μm in diameter) of platy- and needle-shaped crystals (Fig. 8b) that are similar to vivianite crystals recently observed in

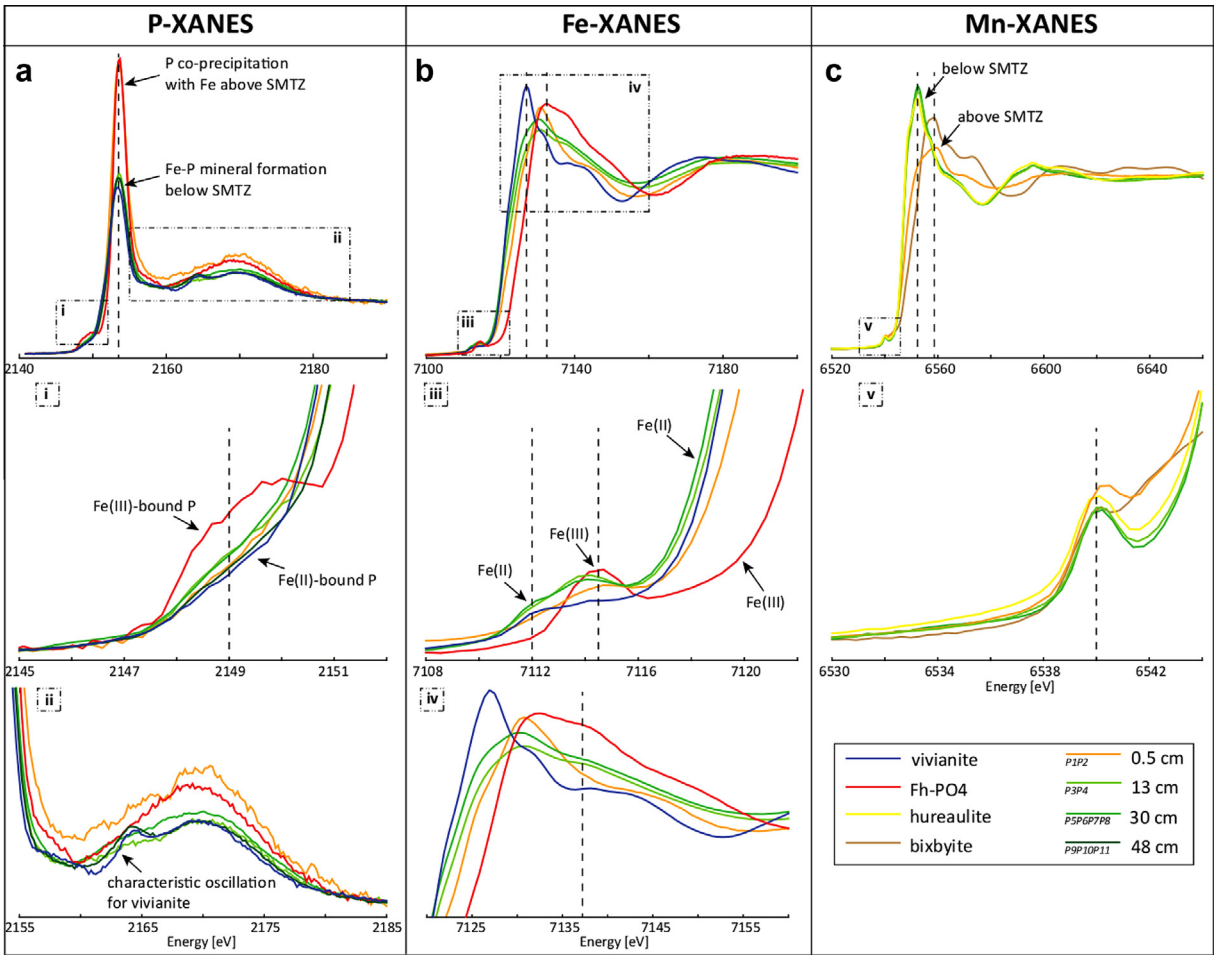

Fig. 7. Focused-beam (1 μm) P (a), Fe (b) and Mn (c) K-edge XANES scans of selected P enrichments at 0.5 cm, 13 cm, 30 cm and 48 cm (P-edge only) depth. P-enrichments within the same depth sample showed only minor variations (Supplementary Fig. S6) and thus were merged together to represent an average sample spectrum for each depth (see legend for points included in the merge). Fh-PO4 represents 2-line ferrihydrite precipitated in the presence of 0.1 M PO_4. In general, Fe–Mn–P enrichments above the SMTZ show different spectra compared to samples from below the SMTZ. P-XANES scans from 48 cm depth show vivianite-like post-edge oscillation.

Lake Ørn, Denmark (O'Connell et al., 2015), with relative Fe to P ratios, derived from EDS analysis approximating those for vivianite (Fig. 8c; Table 2). Additional peaks of Si, Al, Mg and Mn were observed in the EDS spectra of the aggregates. The lack of crystals in sediments above the SMTZ and the absence of any mechanical abrasion features further indicate an authigenic origin.

Electron microprobe-EDS quantitative analyses of these aggregates (Table 2) reveal the presence of significant amounts of Mn (~4–8 wt.%). The relatively high amounts of Si (~2–10 wt.%), Al (~1–5 wt.%) and Mg (~1–3 wt.%) likely reflect remaining clays that were not completely removed during the washing step as visible under the light microscope (Fig. 8a).

The relative amount of Mn incorporated into the Fe–Mn–P aggregates is slightly larger for aggregates collected right below the SMTZ (~6.9 wt.%) compared to samples from the bottom of the sediment core (~5.4 wt.%). This is also reflected in an increased Fe/Mn-ratio and decreased Mn/P-ratio with depth (Table 2). The mean molar Fe/P ratio for samples at the bottom of the SMTZ is 0.82 ± 0.15 and 0.86 ± 0.23 for aggregates at depth, which is close to the molar Fe/P ratio of the synthesized vivianite standard of ~1 using electron microprobe-EDS. The lower measured Fe/P ratio of the vivianite standard compared to the expected stoichiometric ratio for vivianite (Fe/P = 1.5) has been previously reported for vivianite nodules found in marine sediments (Hsu et al., 2014) and could be due to limitations of the semi-quantitative standardless analysis of the EDS spectra applied in this study (Newbury and Ritchie, 2013).

4.3.5. XRD

XRD analyses of sieved sediment from below the SMTZ confirm the presence of Mn-rich vivianite (Fig. 9a). Other Mn- or Fe-bearing phosphate minerals were not recognized in the diffractogram, suggesting that the Fe–Mn–P aggregates analyzed by SEM–EDS indeed represent Mn-rich vivianite. Additional identified peaks, beside vivianite, can be assigned to detrital phases such as illite ((K,H_3O)(Al,

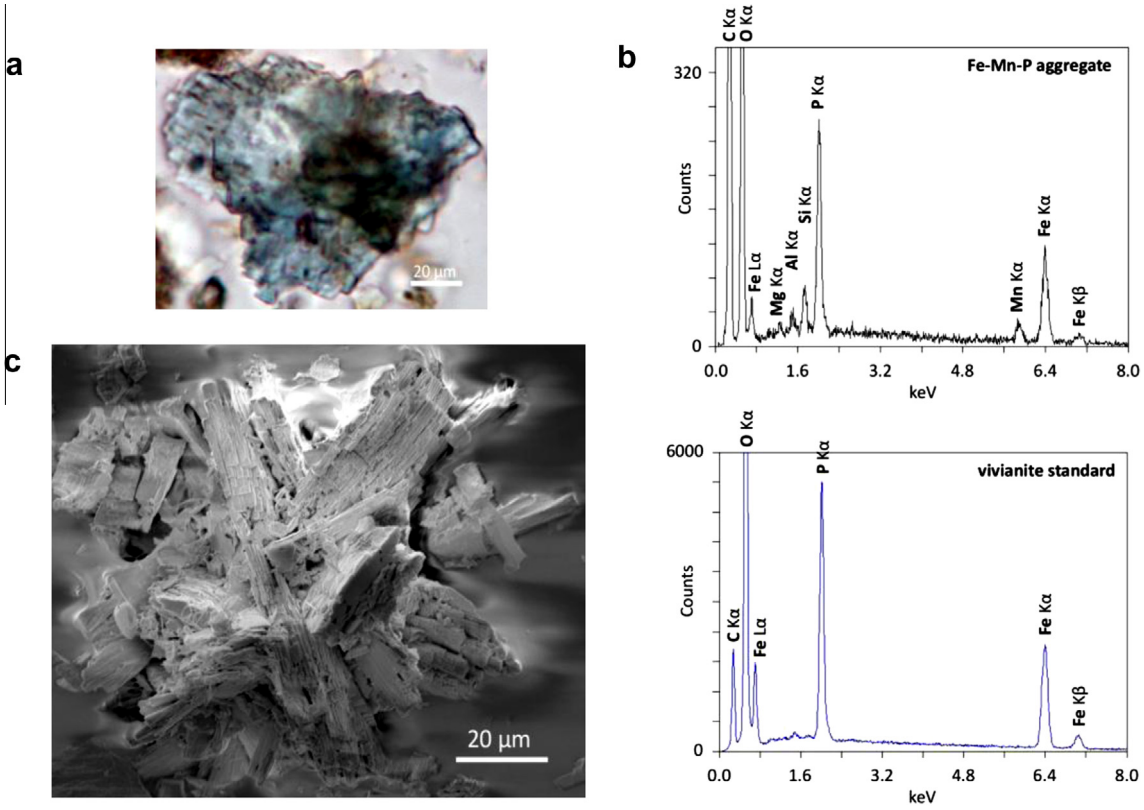

Fig. 8. Examination of sieved (>38 µm) sediment samples from below the SMTZ. (a) Optical light microscopic image of a transparent to light blue crystal. (b) Scanning electron micrograph (SEM) of a blue aggregate from below the SMTZ. (c) Spot-measurement electron microprobe-EDS spectrum on the particle surface (top) and on synthesized vivianite (bottom).

Table 2
Electron microprobe-EDS analyses of vivianite crystals collected from two different sediment depths, i.e. right below the SMTZ ((22 cm, core 2013); $n = 16$) and bottom of the core (58 cm, core 2013); $n = 13$), as well as from synthesized vivianite ($n = 1$).

Element	Unit	Right below SMTZ ($n = 16$)	Bottom of core ($n = 13$)	Vivianite standard
O	[wt.%]	41.48 ± 1.09	41.31 ± 2.06	39.30
Fe	[wt.%]	23.74 ± 2.45	26.14 ± 4.67	38.64
P	[wt.%]	16.25 ± 2.13	17.39 ± 2.60	21.5
Mn	[wt.%]	6.95 ± 1.15	5.35 ± 0.96	0.10
Si	[wt.%]	7.37 ± 2.60	6.11 ± 3.16	0.08
Mg	[wt.%]	2.03 ± 0.59	1.90 ± 0.64	0.04
Al	[wt.%]	2.19 ± 0.69	1.79 ± 1.10	0.31
FeO	[wt.% oxide]	30.54 ± 3.15	33.63 ± 6.01	49.71
P_2O_5	[wt.% oxide]	37.23 ± 4.88	39.85 ± 5.96	49.36
MnO	[wt.% oxide]	8.97 ± 1.48	6.91 ± 1.24	0.13
SiO_2	[wt.% oxide]	15.76 ± 5.57	13.06 ± 6.76	0.17
MgO	[wt.% oxide]	3.36 ± 0.97	3.16 ± 1.06	0.06
Al_2O_3	[wt.% oxide]	4.14 ± 1.31	3.39 ± 2.08	0.58
Fe/Mn	[mol/mol]	3.44 ± 0.64	4.84 ± 0.58	380.10
Fe/P	[mol/mol]	0.82 ± 0.15	0.86 ± 0.23	0.99
(Fe + Mn)/P	[mol/mol]	1.07 ± 0.18	1.03 ± 0.28	1.00
Mn/P	[mol/mol]	0.24 ± 0.05	0.18 ± 0.05	0.00

$Mg,Fe)_2(Si,Al)_4O_{10}((OH)_2,H_2O)$), quartz ($SiO_2$), albite ($NaAlSi_3O_8$) and chlorite ($(Mg,Fe)_6(Si,Al)_4O_{10}(OH)_8$), which agrees well with observations under the light microscope and the SEM results. Some of the diffraction peaks of the sieved sediment are slightly shifted compared to the Mn-free vivianite standard used here. This observation is consistent with previous work on Mn-rich vivianite found in freshwater sediments (Nakano, 1992) (Fig. 9b).

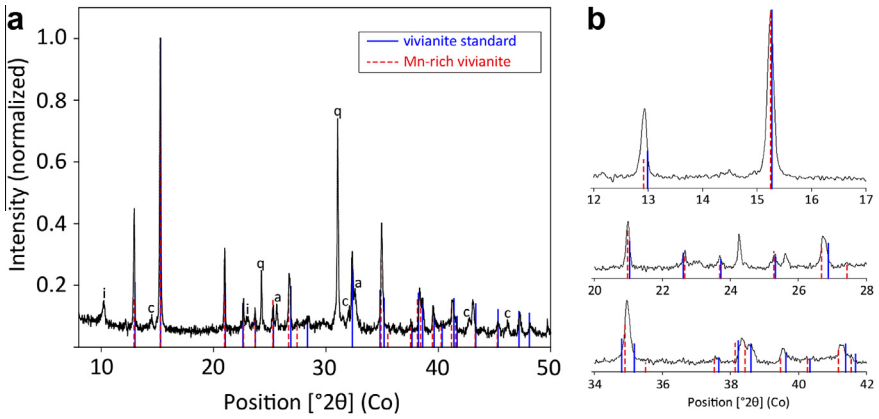

Fig. 9. XRD spectrum of sieved (>38 μm) sediment from below the SMTZ (22 cm, core 2013). (a) The line patterns of synthesized vivianite (blue) and Mn-rich (manganoan) vivianite (red; taken from (Nakano, 1992)) are also plotted. Additional identified peaks, besides vivianite, include detrital phases such as illite (i), quartz (q), albite (a) and chlorites (c). (b) Some of the diffraction peaks of the sieved sediment are slightly shifted compared to the Mn-free vivianite standard used in this study, and generally fall between the line patterns of the Mn-free and the manganoan vivianite. (For interpretation of the references to color in this figure legend, the reader is referred to the web version of this article.)

5. DISCUSSION

5.1. Evidence for vivianite authigenesis

Vivianite authigenesis in aquatic sediments is favored by high pore water concentrations of HPO_4^{2-} and Fe^{2+} and low levels of sulfide (Nriagu, 1972). In most brackish and marine coastal sediments, the presence of dissolved SO_4^{2-} will stimulate microbial SO_4^{2-} reduction and generate dissolved sulfide, ultimately removing Fe^{2+} from the pore water through Fe-sulfide precipitation (Raiswell and Canfield, 2012) and thus limiting vivianite formation in these sediments (Ruttenberg, 2003).

At our study site in the Bothnian Sea, pore water HPO_4^{2-} shows a strong decline with depth in the presence of abundant Fe^{2+}, suggesting authigenic Fe(II)–P formation below the SMTZ. Sequential P extractions further show that Fe-bound P accounts for up to ~60% of the total reactive P burial. Authigenic Ca–P contents, in contrast, are low (~20% of total P burial) and mostly constant with depth, suggesting an allochthonous origin and restricted in-situ formation (Fig. 4a). These results strongly indicate that sink-switching of organic or Fe-bound P to authigenic Ca–P is not controlling reactive P burial at this site, as observed previously for different brackish and marine depositional environments (März et al., 2008; Mort et al., 2010; Slomp et al., 2013).

The stoichiometric ratio of Fe-oxides/Fe-bound P of ~7 at the SWI (Fig. 4) is close to typical ratios reported for oxic marine surface sediments of ~10 (Slomp et al., 1996b). Except for the single sample at the base of the SMTZ, Fe-oxides/Fe-bound P ratios are substantially lower below the SMTZ (~3.5–4.5), indicating a different burial phase for Fe-bound P at depth. Abundant dissolved Fe^{2+} (>1.8 mmol/L) and an increase in Fe-bound P below the SMTZ suggest formation of Fe(II)–P minerals as an additional sink for dissolved HPO_4^{2-} below the SMTZ. In naturally reducing environments, the most stable and probable Fe–phosphate mineral is vivianite (Nriagu and Dell, 1974). The saturation index (SI) of the pore water with respect to vivianite, calculated using PHREEQC with the LLNL database (Parkhurst and Appelo, 1999) and the solubility constant from Al-Borno and Tomson (Al-Borno and Tomson, 1994), indeed reveals oversaturation of the pore water with respect to vivianite below a depth of 9.5 cm (SI ~3) (Supplementary Fig. S8).

In this study, Fe-bound P was determined with the CDB-step of the SEDEX procedure, which targets the Fe-oxide bound P fraction in the sediment. However, previous studies have shown that reduced Fe(II)–P minerals such as vivianite can also be extracted during the CDB step (Nembrini et al., 1983; Dijkstra et al., 2014). We suggest that the Fe-bound P fraction below the SMTZ thus represents a mixture of Fe-oxide bound P and authigenic Fe (II)–P. The lower stoichiometric Fe/P ratio of authigenic vivianite (1.5) relative to buried Fe-oxides (~7 assuming no alteration from the value at the SWI) thus potentially explains the lower Fe/P ratios observed below the SMTZ.

Abundant 50–100 μm scale enrichments in Fe, Mn and P observed in the epoxy resin-embedded sub-cores (Fig. 5 and 6) suggest the presence of Fe–Mn–phosphates below the SMTZ. The high correlation between Fe and P supports the findings of the sequential extractions that Fe-bound P represents an important burial phase for P. μXANES spectra collected at the P, Fe and Mn K-edges (Fig. 7) further reveal that the Fe–Mn–P enrichments from above the SMTZ are distinctly different from samples from below the SMTZ. These differences in the μXANES spectra support the conclusion that the aggregates in sediments below the SMTZ are authigenically formed.

The μXANES spectra demonstrate that the Fe–Mn–P aggregates from below the SMTZ predominantly consist of Fe(II)–Mn(II)–phosphates. SEM–EDS spot-measurement (Fig. 8c) and XRD spectra for sieved sediment samples (Fig. 9) strongly suggest that the Fe–Mn–P aggregates represent Mn-rich vivianite crystals that form below the SMTZ.

The pre-edge peaks observed in the μXANES at the P and Fe K-edges indicating a mixture of Fe(II) and Fe(III) (Wilke et al., 2001; Ingall et al., 2011) thus likely reflect slight oxidation artifacts during sample treatment or interference with oxidized Fe phases in the sediment matrix such as Fe-oxides and Fe-silicates. The fact that the P pre-edge peaks and the Fe pre-edge peak at 7114.5 eV are more pronounced for measurements performed in 2015 (at DLS) compared to samples analyzed in 2013 and 2014 (at ESRF) suggests those pre-edge peaks to mainly be the result of slight oxidation of the samples during storage or wet-sieving. Further evidence for the oxidation of the samples between the analysis at ESRF and DLS is given by the changes in the Fe-XANES post-edge features (oscillation around 7137 eV), reflecting a switch from previously reduced Fe(II)–phosphates to more oxidized Fe(III)–P. We also observed a slight color shift of the crystals from light to dark blue between the analyses at ESRF and DLS, indicating vivianite oxidation. Another possible explanation for the observed sample oxidation, however, could be radiation damage due to the longer exposure time during analysis at the DLS.

The μXANES of the blue crystals in the sieved fraction and of Fe–Mn–P enrichments in the resin-embedded sediment samples are almost identical, with the exception of the oxidation artefacts described above (Supplementary Fig. S7). We therefore conclude that the Fe–Mn–P enrichments observed in the resin-embedded sub cores represent the same blue crystals analyzed by SEM–EDS and XRD. Synchrotron-based microanalysis of resin-embedded subcores thus may provide a helpful tool to study P burial in sedimentary systems where P enrichments are too small to be isolated by sieving.

The similarity of the Mn-XANES spectra of the enrichments below the SMTZ with the Mn(II) phosphate spectrum indicates that Mn(II) is bound to phosphate in the studied mineral specimens. The high amounts of Mn compare well to Mn-rich vivianite nodules found in sediments of Lake Baikal (Fagel et al., 2005; Sapota et al., 2006) and to a Mn-rich vivianite crystal from Lake Biwa (Nakano, 1992). The Fe–Mn–P aggregates formed under the brackish conditions at our study site are thus more similar to authigenic vivianite found in freshwater sediments than to Mg-rich nodules reported for marine systems (Hsu et al., 2014). Incorporation of Mn likely results in structural changes of the vivianite crystal, as suggested by the slight shifts of the diffraction peaks away from our Mn-free vivianite standard toward the Mn-rich vivianite crystals analyzed by (Nakano, 1992) (Fig. 9b). These structural changes could potentially explain why the vivianite-like oscillations around 2161–2166 eV are not observed in the P-XANES of the sediment samples and why their Fe-XANES deviate substantially from the Fe-XANES of the Mn-free vivianite standard. Interestingly, the sample from 48 cm depth showed P-XANES spectra with the post-edge oscillation characteristic for vivianite, which could be the result of increasing Fe/Mn ratios with depth (Table 2) and thus less Mn relative to the amount of Fe in the vivianite structure. Unfortunately, no high-resolution μXRF map was collected at this depth that would allow determination of the corresponding Fe/Mn ratio and to compare it to the shallower samples from 13 cm and 30 cm depth. Thus, additional Fe and P-XANES analyses on synthetic vivianite with incorporation of variable amounts of Mn are needed to conclude whether structural changes are indeed dampening the post-edge oscillation. Another factor that could modify the shape of the XANES spectra is the crystal orientation toward the polarized X-ray beam (Muñoz et al., 2013). While XANES spectra collected on the powdered vivianite standard represent the average signal of the different orientation of multiple crystallites, μXANES collected on single crystals only represent one preferential crystal orientation.

Decreasing amounts of Mn as observed in the deeper vivianite crystals are consistent with increasing ratios of pore water Fe^{2+}/Mn^{2+} toward the bottom of the core (Supplementary Fig. S2). The decrease in Mn could thus reflect constant rates of Fe^{2+} and Mn^{2+} incorporation during crystal growth with depth. Other possible explanations, however, could be the preferential uptake of Fe^{2+} during crystal growth or replacement of Mn^{2+} with Fe^{2+}.

5.2. Importance of vivianite as a burial sink for phosphorus

Our results clearly demonstrate the formation of authigenic Mn-rich vivianite below a shallow SMTZ, supporting an earlier hypothesis that the formation of Fe(II)–P below the zone of SO_4^{2-} reduction might be an important P sink at this site (Slomp et al., 2013). The mean concentrations below the SMTZ of Fe-bound P (~40 μmol/g, Fig. 4a) and Fe-oxides (~150 μmol/g, Fig. 4b) can be used to estimate the quantitative importance of vivianite formation for total P burial in these sediments.

Vivianite has been shown to dissolve in both the hydroxylamine-HCl ("Fe_{ox1}") (Dijkstra et al., 2014) and CDB ("Fe-bound P") steps (Nembrini et al., 1983) of the Fe- and P-extractions applied in this study. Thus, both fractions represent a combination of Fe and P associated with Fe-oxides (Fe_{FeOx} and P_{FeOx}) and vivianite ($Fe_{vivianite}$ and $P_{vivianite}$). The sum of Fe_{FeOx} and $Fe_{vivianite}$ therefore equals the total amount of Fe extracted during the Fe-oxide steps, i.e. 150 μmol/g (Eq. (I)), whereas P_{FeOx} and $P_{vivianite}$ combined are equal to the total Fe-bound P, i.e. 40 μmol/g (Eq. (II)). Assuming a typical stoichiometric ratio of Fe_{FeOx}/P_{FeOx} of 10 (Slomp et al., 1996b) (Eq. (III)), combined with the $Fe_{vivianite}/P_{vivianite}$ ratio of 1.5 (Eq. (IV)), results in a set of 4 equations with 4 unknowns.

$$Fe_{FeOx} + Fe_{vivianite} = 150\ \mu mol/g \quad (I)$$

$$P_{FeOx} + P_{vivianite} = 40\ \mu mol/g \quad (II)$$

$$Fe_{FeOx} = 10P_{FeOx} \quad (III)$$

$$Fe_{vivianite} = 1.5P_{vivianite} \quad (IV)$$

Solving these equations for $P_{vivianite}$, we estimate that about 29 μmol/g of the Fe-bound P is associated with vivianite. If the Fe-oxides/Fe-bound P ratio observed at the sediment surface (~7, Fig. 4) is used as a representation of the P binding capacity of Fe-oxides in these sediments, a lower $P_{vivianite}$ of 24 μmol/g is estimated. Based on the sequential extractions, we therefore conclude that vivianite is responsible for ~40–50% of the total P burial below the

SMTZ, which is higher than a recent estimate for a Danish freshwater lake, where vivianite was suggested to account for ~26% of the total P burial flux using HCl/ascorbic acid reactivity extractions (O'Connell et al., 2015).

An alternative way to quantify the importance of vivianite is to determine the fraction of total P associated with the Fe–Mn–P enrichments based on the Desktop μXRF maps for P. The conceptual idea of this approach is that P concentrations in the vivianite enrichments are higher than in the diffuse P in the matrix, and can be identified as clusters of pixels with elevated P counts. Subsequently, the contribution of pixels within vivianite enrichments to total P counts can be estimated and compared to the total P counts in the maps. The approach assumes that count intensities are linearly related to P concentrations.

We defined vivianite enrichments based on two criteria. Firstly, a cluster of pixels with elevated P counts must be larger than 2 × 2 pixels. Smaller clusters and individual pixels with detectable P were thus considered to contain only diffuse P. Secondly, the pixels within the cluster must have a P count intensity above a certain threshold (see Supplementary Fig. S9 for the determination of the corresponding count intensity threshold). ImageJ software can then be used to calculated the contribution to total P counts of all pixels falling both above the threshold and in the >2 × 2 pixels clusters (i.e. satisfying both criteria).

Using this approach, we estimate that the contribution of the vivianite enrichments to total P burial increases from 38% right below the SMTZ to 46% at depth (Supplementary Fig. S9). Such an increase from 38% to 46% is consistent with an increased abundance of these vivianite enrichments with depth (Fig. 5). Although this value might be underestimated, as adsorption of P fluorescence in the Fe- and Mn-rich aggregates is higher than in the background containing lighter elements, it is in good agreement with the estimate based on the sequential extractions (i.e. ~40–50%). We therefore conclude that the formation of vivianite may account for almost half of the permanent burial of total P, supporting recent studies suggesting that the importance of authigenic Fe(II)–P minerals in coastal systems might be larger than previously thought (Slomp et al., 2013; Jilbert and Slomp, 2013; Dijkstra et al., 2014).

Substantial burial of P as vivianite has implications for the coupled cycling of Fe, P and S in sediments. Previous studies have shown that increased SO_4^{2-} reduction and subsequent formation of Fe-sulfides lower the availability of Fe for binding P in sediments, resulting in more P release to bottom waters and accelerated water column eutrophication (Rozan et al., 2002; Gächter and Müller, 2003). However, the lower stoichiometric Fe/P ratio of vivianite implies that sequestration of P as Fe(II)–P requires less Fe compared to Fe(III)–P burial. This lower requirement for Fe may thus reduce the impact of increased SO_4^{2-} reduction on P retention in the sediment (Slomp et al., 2013). Throughout the last century, anthropogenic eutrophication has enhanced primary production and subsequent export production of organic matter to the Bothnian Sea (Fleming-Lehtinen et al., 2008; Fleming-Lehtinen and Laamanen, 2012), ultimately increasing the rates of SO_4^{2-} reduction in the underlying sediments. Burial of P in the form of vivianite instead of Fe-oxide bound P may therefore have reduced the impact of increased rates of SO_4^{2-} reduction and Fe-sulfide formation on P retention in the sediment, thus increasing sedimentary P burial and acting as a negative feedback on water column eutrophication.

Earlier work has shown that Bothnian Sea sediments are a major burial sink for P originating from the severely eutrophic Baltic Proper (Savchuk, 2005; Slomp et al., 2013), one of the world's largest anoxic water bodies. Because it accounts for almost half of the total P burial in these sediments, vivianite may act as an important permanent P sink not only for the Bothnian Sea itself, but also for P exported from the Baltic Proper.

5.3. Role of anaerobic oxidation of methane (AOM) for vivianite authigenesis

CH_4 plays a key role in providing conditions that allow the formation of vivianite at our study site (Fig. 10). Fluxes of downward diffusing SO_4^{2-} (2.5 mmol m^{-2} d^{-1}) and upward diffusing CH_4 (1.6 mmol m^{-2} d^{-1}) into the SMTZ suggest that about 65% of SO_4^{2-} reduction is associated with AOM coupled to SO_4^{2-} reduction, with the remaining 35% being coupled to organic matter degradation. SO_4^{2-}-mediated AOM thus contributes significantly to the production of sulfide within the SMTZ. The accumulation of dissolved sulfide ultimately results in the reductive dissolution of Fe-oxides and the precipitation of Fe-sulfides (mostly FeS) within the SMTZ. In addition to the conversion of reactive Fe from oxide toward sulfide phases, reduction of Fe-oxides by sulfide also releases HPO_4^{2-} into the pore water. Part of the liberated HPO_4^{2-} diffuses upwards toward the SWI, where it is again trapped in the surface sediment as Fe-oxide bound P or escapes to the overlying water. The pore water profile of HPO_4^{2-} further indicates that a major part of the HPO_4^{2-} diffuses downwards where it meets abundant Fe^{2+}, creating pore water conditions that are favorable for the precipitation of vivianite below the SMTZ. SO_4^{2-}-dependent AOM thus ultimately results in the liberation of formerly Fe-oxide bound P into the pore water and diffusion of dissolved HPO_4^{2-} away from the SMTZ. The role of the SMTZ as a source of HPO_4^{2-} to the pore waters, and the presence of a sink for this HPO_4^{2-} below the SMTZ unrelated to Ca–P authigenesis has also been suggested previously in marine environments (Schulz et al., 1994; Burns, 1997; März et al., 2008) and is thus likely to represent a prevalent feature in many different types of aquatic sediments.

The distinct enrichment of authigenic Fe-sulfides around the present day SMTZ has been suggested to be the result of a recent upward displacement of the SMTZ caused by higher primary productivity and enhanced subsequent export production of autochthonous organic matter (Slomp et al., 2013; Egger et al., 2015) driven by anthropogenic eutrophication over past decades (Fleming-Lehtinen et al., 2008; Fleming-Lehtinen and Laamanen, 2012). Since the early 2000s, anthropogenic loading of nutrients derived from land has started to decline again (Fleming-Lehtinen et al., 2008; Fleming-Lehtinen and Laamanen, 2012). The associated reduced input of organic

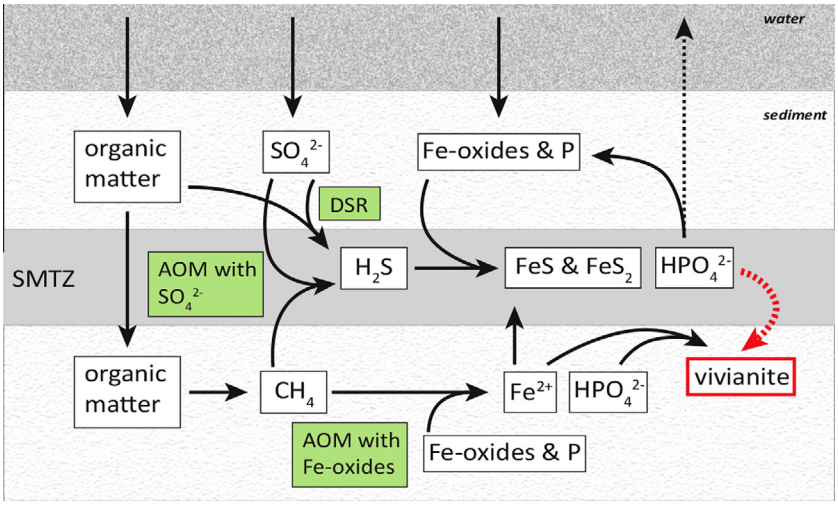

Fig. 10. Model of coupled Fe–S–P–CH_4 dynamics in and below the SMTZ in the Bothnian Sea (adapted from Slomp et al. (2013)). Anaerobic oxidation of CH_4 (AOM) drives a sink-switching from Fe-oxide bound P to vivianite by triggering the release of both HPO_4^{2-} (AOM with SO_4^{2-} and Fe-oxides) and Fe^{2+} (AOM with Fe-oxides), thereby providing conditions that allow sequestration of a major proportion of P as vivianite below the SMTZ. Fe-AOM below the SMTZ provides an additional source of dissolved Fe^{2+} at depth, ultimately reducing the diffusive upward HPO_4^{2-} flux and thus the potential escape of HPO_4^{2-} to the water column. The formation of vivianite below the SMTZ could therefore potentially act as a feedback preventing P release from the sediment and further eutrophication of anthropogenically impacted coastal systems. DSR = dissimilatory sulfate reduction.

matter likely contributes to the lack of a further upward movement of the SMTZ and its fixation at its current position close to the sediment surface (Slomp et al., 2013; Egger et al., 2015). The rapid upward migration of the SMTZ in response to eutrophication reduced the exposure time of sedimentary Fe-oxides to dissolved sulfide, explaining the high Fe-oxide content (~150 μmol/g) in the methanogenic sediments below the current SMTZ. The newly established co-occurrence of abundant reducible Fe-oxides and pore water CH_4 facilitated a potential coupling between AOM and Fe reduction (Fe-AOM) (Beal et al., 2009; Sivan et al., 2011; Segarra et al., 2013; Riedinger et al., 2014; Egger et al., 2015). Laboratory incubation studies with sediments from site US5B and modeling of the isotopic composition of pore water CH_4 identified Fe-AOM to be the most likely mechanism responsible for the high dissolved Fe^{2+} concentrations observed below the SMTZ (Egger et al., 2015). Although most of the CH_4 produced in the sediments is efficiently consumed by SO_4-AOM within the SMTZ (Egger et al., 2015), Fe-AOM strongly contributes to Fe^{2+} production due to the 8:1 Fe-CH_4 stoichiometry (Beal et al., 2009). The reduction of large quantities of Fe-oxides by Fe-AOM below the SMTZ thus provides an important source of dissolved Fe^{2+} for vivianite authigenesis. Besides Fe-oxides, Mn-oxides have also been shown to be thermodynamically favorable electron acceptors for the biological oxidation of CH_4 (Beal et al., 2009). Elevated Mn^{2+} concentrations below the SMTZ could thus indicate AOM coupled to the reduction of Mn-oxides. Further research is needed to investigate whether the incorporation of this Mn^{2+} into vivianite and its associated structural changes, as suggested by our μXANES and XRD results, may promote vivianite precipitation and protection toward sulfidization through enhanced stability.

If Fe-AOM below the SMTZ was absent, most of the Fe-oxide bound P at depth would likely still be retained in the sediment. However, a much larger proportion of the HPO_4^{2-} released from Fe-oxides within the SMTZ would diffuse upwards and escape to the water column. The reason for this is that the additional source of dissolved Fe^{2+} from below would be switched off and most Fe in the SO_4^{2-}-reducing zone would be sequestered in Fe-sulfides, reducing the Fe-oxides available for retention of P. CH_4 thus drives a sink-switching from Fe-oxide bound P to a more stable Fe(II)–P burial phase (i.e. vivianite) by triggering the release of both HPO_4^{2-} (AOM with SO_4^{2-} and Fe-oxides) and Fe^{2+} (AOM with Fe-oxides), thereby providing conditions that allow sequestration of a major proportion of P as vivianite below the SMTZ.

Vivianite authigenesis below the SMTZ requires significant amounts of reactive Fe-oxides to be buried below the zone of SO_4^{2-} reduction. Such conditions are mainly found in systems with a high input of Fe-oxides or where the sediments are subject to transient diagenesis. Non-steady state depositional regimes have been described for a variety of marine systems and formation of vivianite was suggested as a sink for reactive P in these deep sediments (Schulz et al., 1994; Burns, 1997; Riedinger et al., 2005; März et al., 2008; Hsu et al., 2014). Since many deltaic and estuarine types of sediment are naturally rich in Fe-oxides and low in SO_4^{2-}, and may additionally be subject to shifts in the SMTZ linked to eutrophication, vivianite formation may not only be restricted to deep marine sediments with non-steady state diagenetic conditions but also be widespread in coastal surface sediments. If so, vivianite could represent

an important burial sink at the global scale (Ruttenberg, 2003).

6. CONCLUSIONS

Combining the SEDEX sequential extraction method for phosphorus (P) with microscopic and spectroscopic techniques such as Desktop μX-ray fluorescence (μXRF) elemental mapping and synchrotron-based microanalysis (μXRF and X-ray absorption near-edge structure, XANES) of resin-embedded sediments, as well as scanning electron microscope–energy dispersive spectroscopy (SEM–EDS) and powder X-ray diffraction (XRD) of wet-sieved sediment samples, we demonstrate that vivianite formation may account for 40–50% of the total P burial in coastal surface sediments of the Bothnian Sea. Authigenic vivianite crystals are found below a shallow sulfate/methane transition zone (SMTZ) at >10 cm depth and contain significant amounts of manganese (Mn) (~4–8 wt.%), similar to vivianite obtained from freshwater sediments. μXANES spectra collected at the P-, iron (Fe)- and Mn K edges and XRD analysis suggest that the incorporation of Mn into the vivianite results in structural changes of the vivianite structure.

Our results further indicate that anaerobic oxidation of methane drives a sink-switching from Fe-oxide bound P to vivianite. Methane therefore may play a key role in providing conditions that allow for vivianite authigenesis in coastal surface sediments. The depth of vivianite formation seems to be ultimately determined by the location of the SMTZ in the sediments. Coastal eutrophication can induce a vertical upward migration of the SMTZ within the sediment, shifting the zone of favorable conditions for vivianite formation closer to the sediment surface. We thus postulate that anthropogenic fertilization of coastal areas throughout the last century may have increased the role of vivianite authigenesis in many coastal surface sediments. Vivianite therefore likely represents an important burial sink for P in coastal systems worldwide that has so far largely been ignored.

ACKNOWLEDGMENTS

We thank the captain, crew and scientific participants aboard R/V Aranda in 2012 and 2013 and P. Kotilainen for their assistance with the fieldwork. D. van de Meent, H. de Waard, T. Zalm, A. van Dijk, H. van Aken, T. Bouten and A. van Leeuwen are acknowledged for technical and analytical assistance in Utrecht, and M. Wolthers for assistance with the saturation state calculations. We thank the European Synchrotron Radiation Facility for providing beam time at ID21 (experiment number #ES45 and #ES171) and the Diamond Light Source for providing beam time at I18 (experiment #10358). J. F. W. Mosselmans is acknowledged for his helpful support at beamline I18. P. Kraal is thanked for stimulating discussions. We further thank Erik Smedberg for providing us with the Baltic Sea bathymetric map. This research was funded by ERC Starting Grant 278364 and NWO-Vici Grant 865.13.005 (to C. P. Slomp). Associate Editor Benjamin Van Mooy, Christian März and three other anonymous reviewers are gratefully acknowledged for their insightful comments and suggestions that improved the quality of this paper.

APPENDIX A. SUPPLEMENTARY DATA

Supplementary data associated with this article can be found, in the online version, at http://dx.doi.org/10.1016/j.gca.2015.09.012.

REFERENCES

Al-Borno A. and Tomson M. B. (1994) The temperature dependence of the solubility product constant of vivianite. *Geochim. Cosmochim. Acta* **58**, 5373–5378.

Algesten G., Brydsten L., Jonsson P., Kortelainen P., Löfgren S., Rahm L., Räike A., Sobek S., Tranvik L., Wikner J. and Jansson M. (2006) Organic carbon budget for the Gulf of Bothnia. *J. Mar. Syst.* **63**, 155–161.

Beal E. J., House C. H. and Orphan V. J. (2009) Manganese- and iron-dependent marine methane oxidation. *Science* **325**, 184–187.

Burns S. J. (1997) Early diagenesis in Amazon fan sediments. In *Proceeding of the Ocean Drilling Program, Scientific Results* (eds. R. D. Flood, D. J. W. Piper, A. Klaus, and L. C. Peterson). pp. 497–504.

Burton E. D., Sullivan L. A., Bush R. T., Johnston S. G. and Keene A. F. (2008) A simple and inexpensive chromium-reducible sulfur method for acid-sulfate soils. *Appl. Geochem.* **23**, 2759–2766.

Carstensen J., Conley D. J., Bonsdorff E., Gustafsson B. G., Hietanen S., Janas U., Jilbert T., Maximov A., Norkko A., Norkko J., Reed D. C., Slomp C. P., Timmermann K. and Voss M. (2014) Hypoxia in the Baltic Sea: Biogeochemical cycles, benthic fauna, and management. *Ambio* **43**, 26–36.

Cline J. D. (1969) Spectrophotometric determination of hydrogen sulfide in natural waters. *Limnol. Oceanogr.* **14**, 454–458.

Diaz R. J. and Rosenberg R. (2008) Spreading dead zones and consequences for marine ecosystems. *Science* **321**, 926–929.

Dickson A. G., Afghan J. D. and Anderson G. C. (2003) Reference materials for oceanic CO_2 analysis: a method for the certification of total alkalinity. *Mar. Chem.* **80**, 185–197.

Dijkstra N., Kraal P., Kuypers M. M. M., Schnetger B. and Slomp C. P. (2014) Are iron-phosphate minerals a sink for phosphorus in anoxic Black Sea sediments? *PLoS ONE* **9**, e101139.

Egger M., Rasigraf O., Sapart C. J., Jilbert T., Jetten M. S. M., Röckmann T., van der Veen C., Banda N., Kartal B., Ettwig K. F. and Slomp C. P. (2015) Iron-mediated anaerobic oxidation of methane in brackish coastal sediments. *Environ. Sci. Technol.* **49**, 277–283.

Fagel N., Alleman L. Y., Granina L., Hatert F., Thamo-bozso E., Cloots R. and Andre L. (2005) Vivianite formation and distribution in Lake Baikal sediments. *Global Planet. Change* **46**, 315–336.

Filippelli G. M. (1997) Controls on phosphorus concentration and accumulation in oceanic sediments. *Mar. Geol.* **139**, 231–240.

Fleming-Lehtinen V. and Laamanen M. (2012) Long-term changes in secchi depth and the role of phytoplankton in explaining light attenuation in the Baltic Sea. *Estuar. Coast. Shelf Sci.* **102–103**, 1–10.

Fleming-Lehtinen V., Laamanen M., Kuosa H., Haahti H. and Olsonen R. (2008) Long-term development of inorganic nutrients and chlorophyll alpha in the open northern Baltic Sea. *Ambio* **37**, 86–92.

Gächter R. and Müller B. (2003) Why the phosphorus retention of lakes does not necessarily depend on the oxygen supply to their sediment surface. *Limnol. Oceanogr.* **48**, 929–933.

Hsu T.-W., Jiang W.-T. and Wang Y. (2014) Authigenesis of vivianite as influenced by methane-induced sulfidization in cold-

seep sediments off southwestern Taiwan. *J. Asian Earth Sci.* **89**, 88–97.

Ingall E. D., Brandes J. A., Diaz J. M., de Jonge M. D., Paterson D., McNulty I., Elliott W. C. and Northrup P. (2011) Phosphorus K-edge XANES spectroscopy of mineral standards. *J. Synchrotron Radiat.* **18**, 189–197.

Jilbert T. and Slomp C. P. (2013) Iron and manganese shuttles control the formation of authigenic phosphorus minerals in the euxinic basins of the Baltic Sea. *Geochim. Cosmochim. Acta* **107**, 155–169.

Jilbert T., de Lange G. and Reichart G.-J. (2008) Fluid displacive resin embedding of laminated sediments: preserving trace metals for high-resolution paleoclimate investigations. *Limnol. Oceanogr. Methods* **6**, 16–22.

Kraal P., Bostick B. C., Behrends T., Reichart G.-J. and Slomp C. P. (2015) Characterization of phosphorus species in sediments from the Arabian Sea oxygen minimum zone: Combining sequential extractions and X-ray spectroscopy. *Mar. Chem.* **168**, 1–8.

Kraal P. and Slomp C. P. (2014) Rapid and extensive alteration of phosphorus speciation during oxic storage of wet sediment samples. *PLoS ONE* **9**, e96859.

Kraal P., Slomp C. P., Forster A. and Kuypers M. M. M. (2009) Pyrite oxidation during sample storage determines phosphorus fractionation in carbonate-poor anoxic sediments. *Geochim. Cosmochim. Acta* **73**, 3277–3290.

Leipe T., Tauber F., Vallius H., Virtasalo J., Uścinowicz S., Kowalski N., Hille S., Lindgren S. and Myllyvirta T. (2010) Particulate organic carbon (POC) in surface sediments of the Baltic Sea. *Geo-Mar. Lett.* **31**, 175–188.

Martens C. S., Berner R. A. and Rosenfeld J. K. (1978) Interstitial water chemistry of anoxic Long Island Sound sediments. 2. Nutrient regeneration and phosphate removal. *Limnol. Oceanogr.* **23**, 605–617.

März C., Hoffmann J., Bleil U., de Lange G. J. and Kasten S. (2008) Diagenetic changes of magnetic and geochemical signals by anaerobic methane oxidation in sediments of the Zambezi deep-sea fan (SW Indian Ocean). *Mar. Geol.* **255**, 118–130.

Mort H. P., Slomp C. P., Gustafsson B. G. and Andersen T. J. (2010) Phosphorus recycling and burial in Baltic Sea sediments with contrasting redox conditions. *Geochim. Cosmochim. Acta* **74**, 1350–1362.

Muñoz M., Vidal O., Marcaillou C., Pascarelli S., Mathon O. and Farges F. (2013) Iron oxidation state in phyllosilicate single crystals using Fe-K pre-edge and XANES spectroscopy: effects of the linear polarization of the synchrotron X-ray beam. *Am. Mineral.* **98**, 1187–1197.

Nakano S. (1992) Manganoan vivianite in the bottom sediments of Lake Biwa, Japan. *Mineral. J.* **16**, 96–107.

Nembrini G. P., Capobianco J. a., Viel M. and Williams a. F. (1983) A Mössbauer and chemical study of the formation of vivianite in sediments of Lago Maggiore (Italy). *Geochim. Cosmochim. Acta* **47**, 1459–1464.

Newbury D. E. and Ritchie N. W. M. (2013) Is scanning electron microscopy/energy dispersive X-ray spectrometry (SEM/EDS) quantitative? *Scanning* **35**, 141–168.

Nriagu J. O. (1972) Stability of vivianite and ion-pair formation in the system $Fe_3(PO_4)$, $2\text{-}H_3PO_4\text{-}H_2O$. *Geochim. Cosmochim. Acta* **36**, 459–470.

Nriagu J. O. and Dell C. I. (1974) Diagenetic formation of iron phosphates in recent lake sediments. *Am. Mineral.* **59**, 934–946.

O'Connell D. W., Jensen M. M., Jakobsen R., Thamdrup B., Andersen T. J., Kovacs A. and Hansen H. C. B. (2015) Vivianite formation and its role in phosphorus retention in Lake Ørn, Denmark. *Chem. Geol.*

Parkhurst B. D. L. and Appelo C. A. J. (1999) User's Guide To Phreeqc (Version 2)-a Computer Program for Speciation, and Inverse Geochemical Calculations. *Exch. Organ. Behav. Teach. J.* **D**, 326.

Poulton S. and Canfield D. (2005) Development of a sequential extraction procedure for iron: implications for iron partitioning in continentally derived particulates. *Chem. Geol.* **214**, 209–221.

Raiswell R. and Canfield D. E. (2012) The iron biogeochemical cycle past and present. *Geochem. Perspect.* **1**.

Ravel B. and Newville M. (2005) ATHENA, ARTEMIS, HEPHAESTUS: data analysis for X-ray absorption spectroscopy using IFEFFIT. *J. Synchrotron Radiat.* **12**, 537–541.

Riedinger N., Formolo M. J., Lyons T. W., Henkel S., Beck A. and Kasten S. (2014) An inorganic geochemical argument for coupled anaerobic oxidation of methane and iron reduction in marine sediments. *Geobiology* **12**, 172–181.

Riedinger N., Pfeifer K., Kasten S., Garming J. F. L., Vogt C. and Hensen C. (2005) Diagenetic alteration of magnetic signals by anaerobic oxidation of methane related to a change in sedimentation rate. *Geochim. Cosmochim. Acta* **69**, 4117–4126.

Rothe M., Frederichs T., Eder M., Kleeberg a. and Hupfer K. (2014) Evidence for vivianite formation and its contribution to long-term phosphorus retention in a recent lake sediment: a novel analytical approach. *Biogeosciences* **11**, 5169–5180.

Rouzies D. and Millet J. M. M. (1993) Mössbauer study of synthetic oxidized vivianite at room temperature. *Hyperfine Interact.* **77**, 19–28.

Rozan T. F., Taillefert M., Trouwborst R. E., Glazer B. T., Ma S., Herszage J., Valdes L. M., Price K. S. and Iii G. W. L. (2002). *Iron–sulfur–phosphorus cycling in the sediments of a shallow coastal bay: implications for sediment nutrient release and benthic macroalgal blooms.* **47**, 1346–1354.

Ruttenberg K. C. (1992) Development of a sequential extraction method for different forms of phosphorus in marine sediments. *Limnol. Oceanogr.* **37**, 1460–1482.

Ruttenberg K. C. (2003) The global phosphorus cycle. In *Treatise on Geochemistry* (eds. K. K. Turekian and D. J. Holland). Elsevier, pp. 585–643.

Ruttenberg K. C. and Berner R. A. (1993) Authigenic apatite formation and burial in sediments from non-upwelling, continental margin environments. *Geochim. Cosmochim. Acta* **57**, 991–1007.

Ruttenberg K. C. and Goni M. A. (1997) Phosphorus distribution, C:N:P ratios, and d13Coc in arctic, temperate, and tropical coastal sediments: tools for characterizing bulk sedimentary organic matter. *Mar. Chem.* **139**, 123–145.

Salomé M., Cotte M., Baker R., Barrett R., Benseny-Cases N., Berruyer G., Bugnazet D., Castillo-Michel H., Cornu C., Fayard B., Gagliardini E., Hino R., Morse J., Papillon E., Pouyet E., Rivard C., Solé V. A., Susini J. and Veronesi G. (2013) The ID21 Scanning X-ray Microscope at ESRF. *J. Phys: Conf. Ser.* **425**, 182004.

Van Santvoort P. J. M., Lange G. J. D. E., Thomson J., Colley S., Meysman F. J. R. and Slomp C. P. (2002) Oxidation and origin of organic matter in surficial eastern mediterranean hemipelagic sediments. *Aquat. Geochem.* **8**, 153–175.

Sapota T., Aldahan A. and Al-aasm I. S. (2006) Sedimentary facies and climate control on formation of vivianite and siderite microconcretions in sediments of Lake Baikal, Siberia. *J. Paleolimnol.* **36**, 245–257.

Savchuk O. P. (2005) Resolving the Baltic Sea into seven subbasins: N and P budgets for 1991–1999. *J. Mar. Syst.* **56**, 1–15.

Schulz H. D., Dahmke A., Schinzel U., Wallmann K. and Zabel M. (1994) Early diagenetic processes, fluxes, and reaction rates in sediments of the South Atlantic. *Geochim. Cosmochim. Acta* **58**, 2041–2060.

Schwertmann U. and Cornell R. M. (2000) *Iron Oxides in the Laboratory – Preparation and Characterization*. Wiley-VCH, Second, co.

Segarra K. E. A., Comerford C., Slaughter J. and Joye S. B. (2013) Impact of electron acceptor availability on the anaerobic oxidation of methane in coastal freshwater and brackish wetland sediments. *Geochim. Cosmochim. Acta* **115**, 15–30.

Sivan O., Adler M., Pearson A., Gelman F., Bar-Or I., John S. G. and Eckert W. (2011) Geochemical evidence for iron-mediated anaerobic oxidation of methane. *Limnol. Oceanogr.* **56**, 1536–1544.

Slomp C. P., Epping E. H. G., Helder W. and Van Raaphorst W. (1996a) A key role for iron-bound phosphorus in authigenic apatite formation in North Atlantic continental platform sediments. *J. Mar. Res.* **54**, 1179–1205.

Slomp Van., der Gaast S. J. and Van Raaphorst W. (1996b) Phosphorus binding by poorly crystalline iron oxides in North Sea sediments. *Mar. Chem.* **52**, 55–73.

Slomp C. P., Mort H. P., Jilbert T., Reed D. C., Gustafsson B. G. and Wolthers M. (2013) Coupled dynamics of iron and phosphorus in sediments of an oligotrophic coastal basin and the impact of anaerobic oxidation of methane. *PLoS ONE* **8**, e62386.

Stockenberg A. and Johnstone R. W. (1997) Benthic denitrification in the Gulf of Bothnia. *Estuar. Coast. Shelf Sci.* **45**, 835–843.

Strickland J. D. and Parsons T. R. (1972) *A Practical Handbook of Seawater Analysis*. Bulletin 1, Fisheries Research Board of Canada, Ottawa, Canada.

Suess E. (1979) Mineral phases formed in anoxic sediments by microbial decomposition of organic matter. *Geochim. Cosmochim. Acta* **43**, 339–352.

Wilke M., Farges F., Petit P. E., Brown G. E. and Martin F. (2001) Oxidation state and coordination of Fe in minerals: an Fe K-XANES spectroscopic study. *Am. Mineral.* **86**, 714–730.

Associate editor: Benjamin Van Mooy